

# Global temperature projections from a statistical energy balance model using multiple sources of historical data

Mikkel Bennedsen\*, Eric Hillebrand<sup>†</sup> and Jingying Zhou Lykke<sup>‡</sup>

May 23, 2022

## Abstract

This paper estimates the two-component energy balance model as a linear state space system (EBM-SS model) using historical data. It is a joint model for the temperature in the mixed layer, the temperature in the deep ocean layer, and radiative forcing. The EBM-SS model allows for the modeling of non-stationarity in forcing, the incorporation of multiple data sources for the latent processes, and the handling of missing observations. We estimate the EBM-SS model using observational datasets at the global level for the period 1955 – 2020 by maximum likelihood. We show in the empirical estimation and in simulations that using multiple data sources for the latent processes reduces parameter estimation uncertainty. When fitting the EBM-SS model to eight observational global mean surface temperature (GMST) anomaly series, the physical parameter estimates and the GMST projection under Representative Concentration Pathway (RCP) scenarios are comparable to those from Coupled Model Intercomparison Project 5 (CMIP5) models and the climate emulator Model for the Assessment of Greenhouse Gas Induced Climate Change (MAGICC) 7.5. This provides evidence that utilizing a simple climate model and historical records alone can produce meaningful GMST projections.

**Key words:** two-component energy balance model; state space methods; non-stationarity; multiple data sources; historical observations; scenario analysis

---

\*Department of Economics and Business Economics and CREATES, Aarhus University, Fuglesangs Allé 4, 8210 Aarhus V, Denmark. E-mail: [mbennedsen@econ.au.dk](mailto:mbennedsen@econ.au.dk)

<sup>†</sup>Department of Economics and Business Economics and CREATES, Aarhus University, Fuglesangs Allé 4, 8210 Aarhus V, Denmark. E-mail: [ehillebrand@econ.au.dk](mailto:ehillebrand@econ.au.dk)

<sup>‡</sup>Department of Economics and Business Economics and CREATES, Aarhus University, Fuglesangs Allé 4, 8210 Aarhus V, Denmark. E-mail: [jzlykke@econ.au.dk](mailto:jzlykke@econ.au.dk)

# 1 Introduction

In this paper, we propose a state space representation (EBM-SS model) of the two-component energy balance model (EBM) (or two-layer EBM), which is initially introduced in [Paltridge \(1981\)](#) and subsequently extended in [Gregory \(2000\)](#) and [Held et al. \(2010\)](#). Like other versions of EBMs (e.g., [North et al., 1981](#)), the two-component EBM is a simplified mathematical representation of the complicated dynamics underlying temperature changes as energy imbalance between the incoming solar radiation and the outgoing terrestrial radiation for the earth system. It extends the zero-dimensional EBM (e.g., [Budyko, 1969](#); [Sellers, 1969](#); [North et al., 1981](#); [Imkeller, 2001](#)) by accounting for the vertical resolution of the Earth system and two distinct time scales of the global temperature response to external perturbations ([Hasselmann et al., 1993](#); [Held et al., 2010](#); [Geoffroy et al., 2013](#)).

The EBM-SS model enables statistical inference to evaluate parameter estimation uncertainties. Climate modeling is inevitably accompanied with parameter uncertainty (e.g., [Winsberg, 2012](#); [Reyer et al., 2016](#); [Gillingham et al., 2018](#)). Accounting for parameter uncertainty plays a crucial role in obtaining reliable evaluations of climate change and conducting robust projection.

Other approaches to quantify parameter uncertainty for the two-component EBM include sensitivity analysis ([Soldatenko & Colman, 2019](#); [Colman & Soldatenko, 2020](#)), Monte Carlo simulation ([Gillingham et al., 2018](#); [Smith et al., 2018](#); [Jiménez-de-la Cuesta & Mauritsen, 2019](#)), and Bayesian estimation ([Jonko et al., 2018](#); [Nijse et al., 2020](#)). The main drawback of sensitivity analysis is its disconnection with any measure of probability, while Monte Carlo simulation assumes the input parameter estimates as the true values. (e.g., [Cox & Baybutt, 1981](#)). The performance of Bayesian estimation depends on the prior distributions (e.g., [Kim et al., 2020](#)). Alternatively, state space methods obtain maximum likelihood estimators based on the frequentist principle and easily quantify parameter uncertainty using asymptotic properties ([Durbin & Koopman, 2012](#)).

The EBM-SS model reduces estimation uncertainty by using multiple data sources. There are different datasets available for GMST. All of the GMST anomalies series from separate research groups can be regarded as different measurements for the same variable of interest – the temperature in the mixed layer in the two-component EBM. As we will show, employing different data sources reduces information loss and improves estimation accuracy.

The EBM-SS model provides alternatives and extensions to two current contributions by [Pretis \(2020\)](#) and [Cummins et al. \(2020\)](#), who obtain parameter values of the two-component EBM using maximum likelihood. [Pretis \(2020\)](#) shows the mathematical equivalence between the two-component EBM and a cointegrated VAR model (EBM-CVAR). Instead of including the temperature in the deep ocean layer, he includes ocean heat content (OHC) in his model. In his discretization, two of the parameters of the two-component EBM, heat capacity in the mixed layer and the coefficient for the heat transfer, are not recovered in the output EBM-CVAR model. In this paper, we maintain the original parametrization by modeling the temperature in the deep layer but also incorporate OHC as an additional measurement for it, which helps constrain the

parameters. We maintain a one-to-one mapping relationship between the two-component EBM and our state space model so that all of the physical parameters can be estimated and interpreted accordingly.

Cummins et al. (2020) present a state space representation of the  $k$ -layer EBM and report parameter estimates for the cases where  $k = 2$  and  $k = 3$ . Our paper only considers the case  $k = 2$  and differs from Cummins et al. (2020) in several ways: (1) we employ observational datasets instead of the abrupt  $4\times\text{CO}_2$  experiment data from CMIP5; (2) we model radiative forcing as a non-stationary process instead of a stationary red noise process; (3) we use instrumental records of ocean temperature, OHC, and effective radiative forcing instead of top-of-the-atmosphere net downward radiative flux as measurements in the state space model; and (4) we incorporate multiple data sources for the latent states.

In this paper, using historical datasets, we obtain estimates for the physical parameter in the two-component EBM that are comparable to the estimates in Cummins et al. (2020) that are obtained from CMIP5 model outputs. Meanwhile, the GMST projection results under RCP 2.6, RCP 4.5, and RCP 6.0 scenarios have a high degree of agreement with the outputs from the climate emulator MAGICC 7.5 and CMIP5 models. These results require two ingredients. One is the inclusion of multiple historical records as different data sources into the EBM-SS model. The other is the inclusion of both ocean temperature and OHC datasets. Our results indicate that utilizing a simple climate model with historical records alone can produce meaningful physical parameter estimates and GMST projections.

The remainder of the paper is organized as follows: Section 2 presents the two-component EBM. Section 3 describes the method and technical details on mapping the two-component EBM into a state space representation. Section 4 presents simulation results on the performance of the EBM-SS model. Sections 5 and 6 introduce the datasets and their use as measurements in the empirical study. Section 7 contains an application of the EBM-SS model to GMST projections using RCP scenarios. Section 8 concludes.

## 2 Two-component energy balance models

The two-component EBM (e.g., Gregory, 2000; Held et al., 2010) divides the earth system into two thermal reservoirs (also referred to as “layer”, “box”, or “component”) that are characterized by different heat capacities to measure thermal inertia. Each of the reservoirs contains components of global climate responses with both fast and slow time scales.

The first layer is usually called the “mixed layer” and consists of the atmosphere, the land surface, and the upper ocean layer. The second layer is called the “deep ocean layer”. The depth of the upper ocean layer varies seasonally and geographically. Hartmann (2015, Chapter 7) argues that the global mean depth of the ocean in the mixed layer is 70 m. Gregory (2000) considers the upper ocean layer as the part that shows consistent temperature variations with the surface temperature. He chooses 150 m as the depth for the upper layer based on the temporal correlation

between the heating rates of different ocean layers and that of the surface. In addition, he defines 2,400 m as the lower bound for the deep layer and describes the part beyond this level as an “isolated basin”.

Figure 2.1: Dynamics of the two-component EBM

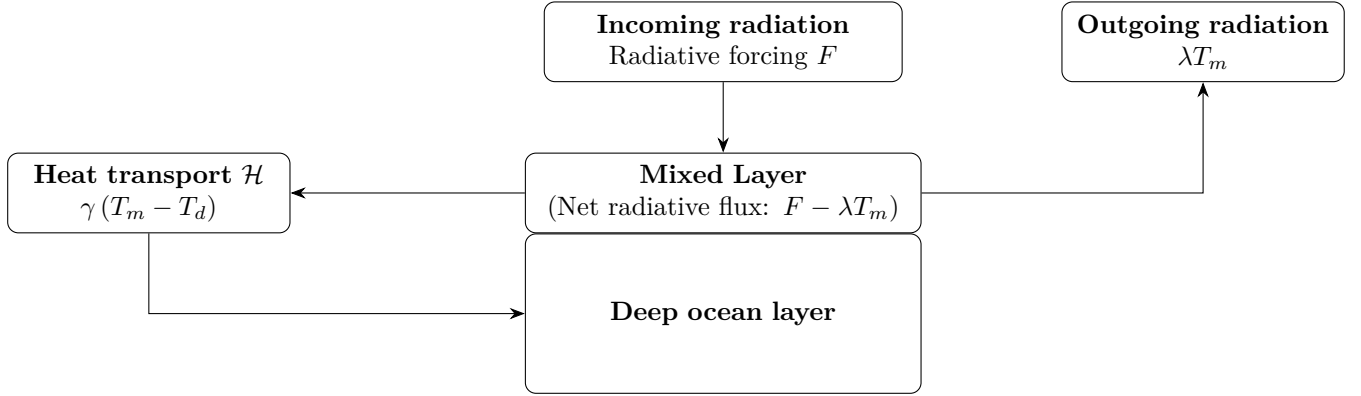


Figure 2.1 gives a graphic illustration of the dynamics underlying the two-component EBM. The change in the heat content of the mixed layer is driven by two sources in opposite directions: external and internal. The external source comes from the net heat flux, which is characterized as  $F - \lambda T_m$ , where the incoming heat radiation is represented by the effective radiative forcing  $F$  (measured in  $\text{Wm}^{-2}$ ), and the outgoing longwave radiation (OLR) is modeled as a linear function of the temperature in the mixed layer  $T_m$  with the slope  $\lambda$  (known as the climate feedback parameter,  $\text{Wm}^{-2}\text{K}^{-1}$ ). The practice of using  $\lambda T_m$  to approximate OLR follows a linear approximation widely used in physical science. The linearity between  $T$  and OLR is validated by satellite measurements and can be explained in physics by the offsetting of two non-linear processes (Koll & Cronin, 2018). The internal source involves a downward heat transport  $\mathcal{H}$  (measured in  $\text{Wm}^{-2}$ ) from the mixed layer to the deep ocean layer, which changes proportionally to the temperature difference  $T_m - T_d$  between these two layers with a coefficient  $\gamma$  ( $\text{Wm}^{-2}\text{K}^{-1}$ ). This term is deemed a reasonable approximation of all of the small perturbations constituting the heat transfer (Gregory, 2000). The heat exchange term,  $\mathcal{H} = \gamma(T_m - T_d)$ , poses the only source of energy for the deep ocean layer. Summarizing the dynamics described in Figure 2.1 into a differential equation system, the two-component EBM is specified as:

$$\begin{aligned} C_m \frac{dT_m}{dt} &= F - \lambda T_m - \gamma(T_m - T_d), \\ C_d \frac{dT_d}{dt} &= \gamma(T_m - T_d), \end{aligned} \tag{2.1}$$

where  $C_m$  and  $C_d$  (measured in  $\text{W year m}^{-2} \text{K}^{-1}$ ) denote heat capacities of the mixed layer and of the deep ocean layer, respectively. It holds that  $C_m < C_d$ , indicating that the deep ocean requires a greater amount of energy than the upper layer for a unit change in the temperature. The terms  $C_m \frac{dT_m}{dt}$  and  $C_d \frac{dT_d}{dt}$  describe the rates at which the corresponding temperatures change. In this

framework, the radiative forcing  $F$  is generated exogenously to the system (e.g., by anthropogenic factors). There are four physical parameters to be estimated:  $\lambda$ ,  $\gamma$ ,  $C_m$ , and  $C_d$ . In the next sections, we map the two-component EBM into a state space model and estimate the values of these physical parameters using maximum likelihood methods.

## 2.1 Including ocean heat content in the system

Ocean heat content (OHC) (measured in  $\text{J m}^{-2}$ ) measures the amount of heat stored in the ocean. Mathematically, ocean heat content  $O$  between ocean depths  $h_1$  and  $h_2$  is calculated as:

$$O = \rho C \int_{h_2}^{h_1} T(x) dx, \quad (2.2)$$

where  $\rho$ ,  $C$ , and  $T(\cdot)$  denote the seawater density, heat capacity, and the temperature at a specific depth, respectively (Dijkstra, 2008). We denote  $\rho C$  as  $C_d$  and  $\int_{h_2}^{h_1} T(x) dx$  as  $T_d$ , which represents the integrated average ocean temperature between  $h_1$  and  $h_2$ . Then, Equation (2.2) is rewritten as:

$$O = C_d T_d. \quad (2.3)$$

This relationship implies the heat content expression  $C_d \frac{dT_d}{dt} = \frac{dO}{dt}$  for the term  $C_d \frac{dT_d}{dt}$  in the two-component EBM (2.1). Relating the temperature to heat content in this way is a common practice in energy balance models, and it is motivated by empirical evidence (Schwartz, 2007).

In our state space model of the two-component EBM introduced later, we include OHC in the measurement equation using the linear relationship  $O = C_d T_d$ . In our specification, OHC plays the role of a second measurement for the latent state  $T_d$ , in addition to the direct empirical observations of  $T_d$  as the first measurement. As shown in Equation (2.2), OHC is a function of the deep ocean temperature, and in practice, the observational OHC series is compiled using the records of ocean temperature data plus salinity information (Levitus et al., 2012). Hence, our choice to include OHC as an additional measurement for  $T_d$  is grounded on both the theory and the empirical data construction process. In Section 6, we will show that using information of both ocean temperature and OHC helps constrain the parameter estimates to be more realistic compared with using ocean temperature alone.

## 3 Mapping the two-component EBM into a state space model

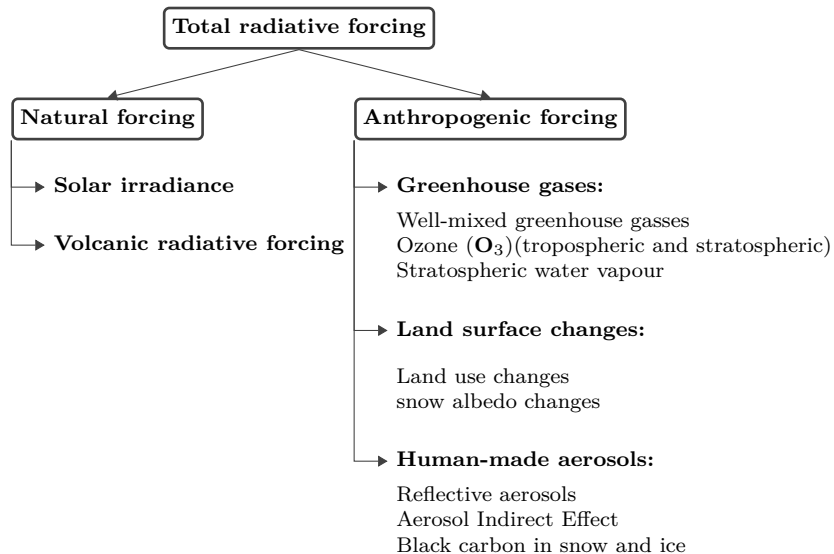
The objective of this section is a discrete-time state space representation of the two-component EBM that enables estimation using empirical data. Particularly, we focus on the multivariate linear Gaussian state space model. For details on the estimation of these models, see Durbin and Koopman (2012). State space models distinguish unobserved states from observations, where the

observations are employed to infer the states. They also allow for using multiple observation series as measures of the latent state of interest.

### 3.1 Decomposition of radiative forcing

We decompose the state of radiative forcing,  $F$ , into two components by source and treat them separately. Total radiative forcing is disaggregated into natural forcing and anthropogenic forcing, where the latter can be further decomposed by the forcing agents. Figure 3.1 shows the decomposition employed in the fifth IPCC assessment report Myhre et al. (2013, Chapter 8). As seen in Figure 3.1, natural forcing is mainly driven by two contributors: solar irradiance and volcanic forcing. Anthropogenic forcing is subject to human influences and consists of forcing from greenhouse gases, land surface changes, and human-made aerosols.

Figure 3.1: Components of radiative forcing

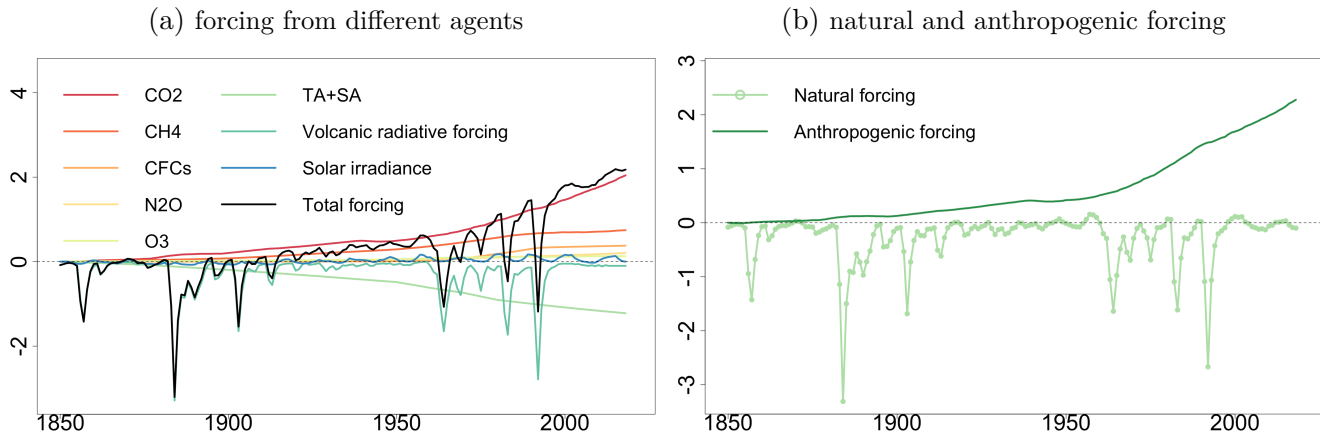


We obtain the latest version of the effective forcing dataset from Hansen et al. (2011) as the measurement for  $F_t$  and show the data in Figure 3.2. It provides information on forcing from different greenhouse gases and summarizes the forcing due to the land surface changes and human-made aerosols into a category “TA+SA” (tropospheric aerosols and surface albedo forcings combined).

As seen in Figure 3.2a, the observation-based natural forcing  $Y_{N,t}$  is dominated by the volcanic forcing, which appears as negative spikes due to temporary cooling periods lasting approximately three years after major volcanic eruptions, while solar irradiance varies around zero over time and exhibits cyclical behavior. Anthropogenic forcing is attributed to human activities, of which the dominant contributors are the well-mixed greenhouse gases. Figure 3.2b shows the two time series for natural forcing and anthropogenic forcing we use in this paper. Natural forcing exhibits large negative spikes and remains otherwise close to zero, while anthropogenic forcing is upward trending.

As natural forcing and anthropogenic forcing have distinct time series characteristics, we treat

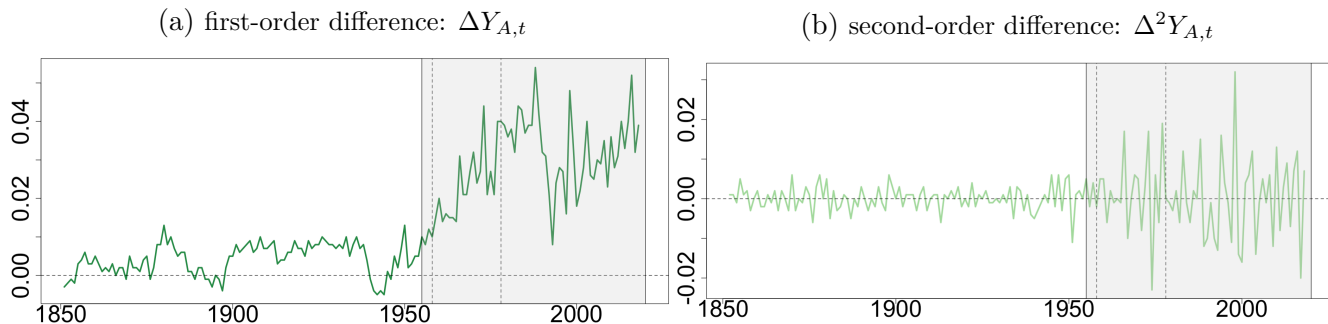
Figure 3.2: Components of radiative forcing (1850 – 2018,  $\text{Wm}^{-2}$ ) from Hansen et al. (2011)



them separately. In our state space model, we let  $F_t = A_t + N_t$ , where  $A_t$  is anthropogenic forcing and  $N_t$  is natural forcing. We model  $A_t$  but we treat  $N_t$  as an exogenous regressor and use historical data for it. Considering the small magnitude of solar irradiance, we do not introduce extra structure to model its cyclical feature explicitly. Anthropogenic greenhouse gas emissions following industrialization increase anthropogenic forcing (denoted as  $Y_{A,t}$ ) and render it non-stationary (Kaufmann et al., 2013; Chang et al., 2020). In the two-component EBM system, the increasing anthropogenic forcing raises temperatures at the surface and in the ocean, thus, temperatures become non-stationary, too. Anthropogenic forcing is external to the system of surface temperature and ocean heat uptake, and, hence, it can be regarded as the major source of non-stationarity in the system. Non-stationarity poses statistical challenges such as spurious regression (e.g., Granger & Newbold, 1974). State space methods can be used to specify systems of non-stationary variates while retaining valid statistical inference (Caines, 1988).

As shown in Figure 3.3a, the first-order difference of anthropogenic forcing,  $\Delta Y_{A,t}$ , appears

Figure 3.3: First and second-order differences of the time series of anthropogenic forcing  $Y_{A,t}$  ( $\text{Wm}^{-2}$ ) during 1850 – 2018. The two vertical dashed lines mark the year 1958 and 1978 when the measurement scheme method changes. The gray area is the time horizon 1955 – 2020 for the empirical study in this paper.



non-stationary with both trends and shifts of trends. The second-order difference in Figure 3.3b exhibits an abrupt increase in variance in the 1950s. The shifts in the trends and the variance are

mainly the result of changes in measurement methods. For example, greenhouse gases are initially measured using ice core records and later measured directly from the atmosphere (e.g., [Raynaud et al., 1993](#)). This switch applies since the year 1958 for CO<sub>2</sub> and 1978 for CH<sub>4</sub> and N<sub>2</sub>O. These structural shifts may indicate the existence of wide-sense non-stationarity in anthropogenic forcing, which invalidates the method of obtaining a stationary process by taking differences ([Castle & Hendry, 2019, 2020](#)). An in-depth analysis of wide-sense non-stationarity is beyond the scope of this paper, but we investigate the integration order of anthropogenic forcing. Unit root test results are reported in [Table A.1](#) in [Appendix A.1](#). As shown in [Table A.1](#), the components of forcing exhibit different integration orders. Total radiative forcing,  $Y_{F,t}$ , is an  $I(1)$  process, i.e., it becomes stationary after taking first-order difference. This observation is consistent with the statement in [Pretis \(2020\)](#) that the individual forcing components integrate to an  $I(1)$  total forcing upon summation. [Table A.1](#) also implies that total anthropogenic forcing,  $Y_{A,t}$ , is an  $I(1)$  process when no lag or only the first-order lag is included in the unit root test equation, but it is an  $I(2)$  process if a higher-order lag is included.

Guided by the unit root tests and visual inspection of  $Y_A$  and its differences, we represent  $A_t$  using a local linear trend model ([Durbin & Koopman, 2012](#), Chapter 3), where  $A_t$  is a random walk process with a stochastic trend  $\beta_t$ :

$$\begin{aligned} A_t &= \beta_t + A_{t-1} + \eta_{A,t}, \\ \beta_t &= \beta_{t-1} + \eta_{\beta,t}, \end{aligned} \tag{3.1}$$

where  $\eta_{A,t}$  and  $\eta_{\beta,t}$  are independent Gaussian white noise processes with variances  $\sigma_{\eta_A}^2$  and  $\sigma_{\eta_\beta}^2$ , respectively. The second-order difference  $\Delta^2 A_t$  is thus a linear function of two white noise processes and hence stationary:<sup>1</sup>

$$\Delta^2 A_t = \eta_{\beta,t} + \eta_{A,t} - \eta_{A,t-1}. \tag{3.2}$$

As a result,  $A_t$  is modeled as an  $I(2)$  process. [Figure 3.3b](#) shows a variance increase and hence suggests the existence of heteroskedasticity in  $\Delta^2 A_t$ . One method to accommodate such a variance shift is to impose a multiplicative constant on the variance of the measurement error of forcing  $\sigma_{\varepsilon, Y_F}^2$  from the year where the measurement scheme shifts onwards, and this constant can be estimated using maximum likelihood. Inclusion of such a constant yielded insignificant estimates on the sample period 1955 – 2020, and hence we omit it from the model.

## 3.2 EBM-State Space (EBM-SS) model – state equation

The state equation in a state space model describes the dynamics of the latent state variables as a first-order autoregressive process. For our EBM-SS model, we define the following five variables as unobservable latent states: the temperature in the mixed layer  $T_m$ , the temperature in the deep

---

<sup>1</sup>If we set  $\sigma_{\eta_A}^2 = 0$ , Equation (3.2) is reduced to  $\Delta^2 A_t = \eta_{\beta,t}$ , which is called integrated random walk model ([Young et al., 1991; Durbin & Koopman, 2012](#)).



ocean layer  $T_d$ , natural forcing  $N$ , anthropogenic forcing  $A$ , and the stochastic trend  $\beta$ .

According to the dynamics in the two-component EBM (differential equation system (2.1)) and the decomposition of  $F$  in Section 3.1, we formulate the state equation system as the following system of linear equations:

$$\begin{aligned}
T_{m,t} &= \left(1 - \frac{(\lambda + \gamma)}{C_m}\right) T_{m,t-1} + \frac{\gamma}{C_m} T_{d,t-1} + \frac{1}{C_m} (N_{t-1} + A_{t-1}) + \eta_{T_{m,t}}, \\
T_{d,t} &= \frac{\gamma}{C_d} T_{m,t-1} + \left(1 - \frac{\gamma}{C_d}\right) T_{d,t-1} + \eta_{T_{d,t}}, \\
N_t &= Y_{N,t}, \\
A_t &= \beta_t + A_{t-1} + \eta_{A,t}, \\
\beta_t &= \beta_{t-1} + \eta_{\beta,t},
\end{aligned} \tag{3.3}$$

where  $\eta_{T_{m,t}}$ ,  $\eta_{T_{d,t}}$ ,  $\eta_{A,t}$ , respectively, and  $\eta_{\beta,t}$  are the state disturbances to the states  $T_{m,t}$ ,  $T_{d,t}$ ,  $A_t$  and  $\beta_t$ , and they capture the deviations from the assumed linear relations implied by the two-component EBM and the local linear trend model (Equation (3.1)). We assume the state disturbances to be independent and  $\eta_{.,t} \sim \mathcal{N}(0, \sigma_{\eta_{.,t}}^2)$ . The system of equations (3.3) allows for modeling non-stationarity. It establishes temperature changes as a response to perturbations in radiative forcing and represents the non-stationarity in radiative forcing using a local linear trend model, which is the only source of a stochastic trend in the system, and the stochastic trend propagates to temperatures at the surface and in the ocean through linear relationships. The equation  $N_t = Y_{N,t}$  captures that we use observational data  $Y_{N,t}$  on natural forcing for the latent process  $N_t$ , i.e., we treat it as exogenous.

### 3.3 EBM-SS model – measurement equation

The measurement equation in a state space model connects the observational data vector to the latent state vector linearly. We consider the following measurement equations:

$$\begin{aligned}
Y_{T_{m,t}} &= T_{m,t} + \varepsilon_{T_{m,t}}, \\
Y_{T_{d,t}} &= T_{d,t} + \varepsilon_{T_{d,t}}, \\
Y_{O,t} &= C_d T_{d,t} + \varepsilon_{O,t}, \\
Y_{F,t} &= N_t + A_t + \varepsilon_{F,t},
\end{aligned} \tag{3.4}$$

where  $Y_{*,t}$  denotes the measurement for the latent process  $*$ . Following the assumption  $O = C_d T_d$ , the third equation in (3.4) expresses the OHC series,  $Y_{O,t}$ , as an alternative measurement for  $T_d$ . Note that the data for  $Y_{O,t}$  and  $Y_{T_{d,t}}$  are retrieved from the same institution and cover the same ocean depth. We assume that  $\varepsilon_{.,t} \sim \mathcal{N}(0, \sigma_{\varepsilon_{.,t}}^2)$ , and the correlation  $\text{Corr}(\varepsilon_{T_{d,t}}, \varepsilon_{O,t}) = \rho$ , where  $\rho$  can be estimated using maximum likelihood like other parameters. Allowing for correlation between the measurement errors of ocean temperature and OHC accounts for the highly correlated data

compilation processes for these two series.

### 3.3.1 Incorporation of multiple measurements

Cummins et al. (2020) fit a two-box EBM to datasets from 16 Earth System Models (ESMs) in CMIP5 separately and further consider a joint data series that is the average of these 16 datasets. The parameter estimates vary across different datasets due to the heterogeneity of the ESMs. We employ an alternative strategy. We include different data sources simultaneously in the measurement equation as multiple measurements for the latent states. This approach only produces one set of parameter estimates regardless of the number of measurements we include. We focus on using multiple data sources of GMST, ocean temperature, and OHC.<sup>2</sup> The two latent processes  $T_{m,t}$  and  $T_{d,t}$  are linearly linked to multiple observational measurements. For example, the  $K$  ( $K \in \mathbb{N}$ ) GMST anomalies  $Y_{T_m,t}^1, \dots, Y_{T_m,t}^K$  share the same driver – the latent process  $T_{m,t}$ . They are distinguished from each other by separate measurement errors  $\varepsilon_{T_m,t}^1, \dots, \varepsilon_{T_m,t}^K$ . For ocean temperature and OHC, we include series from the same institution in pairs, as they are correlated measurements for  $T_d$ . The measurement equations that include  $J$  and  $K$  ( $J \in \mathbb{N}$ ) data sources for GMST and ocean data are formulated as:

$$\begin{aligned}
Y_{T_m,t}^1 &= T_{m,t} + \varepsilon_{T_m,t}^1, \\
&\vdots \\
Y_{T_m,t}^K &= T_{m,t} + \varepsilon_{T_m,t}^K, \\
Y_{T_d,t}^1 &= T_{d,t} + \varepsilon_{T_d,t}^1, & Y_{O,t}^1 &= C_d T_{d,t} + \varepsilon_{O,t}^1, \\
&\vdots & &\vdots \\
Y_{T_d,t}^J &= T_{d,t} + \varepsilon_{T_d,t}^J, & Y_{O,t}^J &= C_d T_{d,t} + \varepsilon_{O,t}^J, \\
Y_{F,t} &= N_t + A_t + \varepsilon_{F,t}.
\end{aligned}$$

Similar to the one-data-source case,  $\varepsilon_{T_m,t}^k \sim \mathcal{N}\left(0, \sigma_{\varepsilon, Y_{T_m,t}^k}^2\right)$ ,  $\varepsilon_{T_d,t}^j \sim \mathcal{N}\left(0, \sigma_{\varepsilon, Y_{T_d,t}^j}^2\right)$ ,  $\varepsilon_{O,t}^j \sim \mathcal{N}\left(0, \sigma_{\varepsilon, Y_{O,t}^j}^2\right)$ ,  $\varepsilon_{F,t} \sim \mathcal{N}\left(0, \sigma_{\varepsilon, Y_F}^2\right)$ , and  $\text{Corr}\left(\varepsilon_{T_d,t}^j, \varepsilon_{O,t}^j\right) = \rho_j$ .

## 3.4 EBM-SS model – matrix form

In this section, we integrate Section 3.2 and Section 3.3 and present the matrix form of the EBM-SS model. We only discuss the specification with multiple data sources, which nests the one-data-source case. We denote  $\mathbf{X}_t = \left(T_{m,t} \ T_{d,t} \ N_t \ A_t \ \beta_t \ 1\right)^\top$  as the state vector and  $\mathbf{Y}_t = \left(Y_{T_m,t}^1 \ \dots \ Y_{T_m,t}^K \ Y_{T_d,t}^1 \ \dots \ Y_{T_d,t}^J \ Y_{O,t}^1 \ \dots \ Y_{O,t}^J \ Y_{F,t}\right)^\top$  as the observational vector. The processes in  $X_t$  are unobserved, with the exceptions of natural forcing  $N_t$  and the constant state

<sup>2</sup>We use one data source for radiative forcing. This is because we could not find an alternative observation-based dataset that provides complete information on the total radiative forcing and its components as the one by Hansen et al. (2011).

“1”. The latter is a technical way to equate the state  $N_t$  with observations  $Y_{N,t}$  without errors, or in other words, to treat them as an exogenous regressor, as seen in Equation (3.6). The observational vector contains data on the elements of the state vector and on OHC ( $Y_{O,t}^1, \dots, Y_{O,t}^J$ ). We write the state disturbances into a vector  $\boldsymbol{\eta}_t = \left( \eta_{T_m,t} \quad \eta_{T_d,t} \quad 0 \quad \eta_{A,t} \quad \eta_{\beta,t} \quad 0 \right)^\top$  and the measurement errors into a vector  $\boldsymbol{\varepsilon}_t = \left( \varepsilon_{T_m,t}^1 \quad \dots \quad \varepsilon_{T_m,t}^K \quad \varepsilon_{T_d,t}^1 \quad \dots \quad \varepsilon_{T_d,t}^J \quad \varepsilon_{O,t}^1 \quad \dots \quad \varepsilon_{O,t}^J \quad \varepsilon_{F,t} \right)^\top$ , where the two 0's in  $\boldsymbol{\eta}_t$  are due to the absence of state disturbances for the natural forcing state and the constant state. The EBM-SS model is written as a standard discrete-time state space form, as defined in, e.g., [Durbin and Koopman \(2012\)](#):

$$\begin{aligned} \mathbf{X}_{t+1} &= \mathbf{T}\mathbf{X}_t + \boldsymbol{\eta}_t, & \boldsymbol{\eta}_t &\sim \mathcal{N}(0, \mathbf{Q}), \\ \mathbf{Y}_t &= \mathbf{Z}\mathbf{X}_t + \boldsymbol{\varepsilon}_t, & \boldsymbol{\varepsilon}_t &\sim \mathcal{N}(0, \mathbf{H}). \end{aligned} \quad (3.5)$$

The matrices  $\mathbf{T}$ ,  $\mathbf{Q}$ ,  $\mathbf{H}$ , and  $\mathbf{Z}$  are time-invariant. The state equation  $\mathbf{X}_{t+1} = \mathbf{T}\mathbf{X}_t + \boldsymbol{\eta}_t$  is written explicitly as:

$$\begin{pmatrix} T_{m,t+1} \\ T_{d,t+1} \\ N_{t+1} \\ A_{t+1} \\ \beta_{t+1} \\ 1 \end{pmatrix} = \begin{pmatrix} \frac{-(\lambda+\gamma)}{C_m} + 1 & \frac{\gamma}{C_m} & \frac{1}{C_m} & \frac{1}{C_m} & 0 & 0 \\ \frac{\gamma}{C_d} & -\frac{\gamma}{C_d} + 1 & 0 & 0 & 0 & 0 \\ 0 & 0 & 0 & 0 & 0 & Y_{N,t+1} \\ 0 & 0 & 0 & 1 & 1 & 0 \\ 0 & 0 & 0 & 0 & 0 & 1 \\ 0 & 0 & 0 & 0 & 0 & 1 \end{pmatrix} \begin{pmatrix} T_{m,t} \\ T_{d,t} \\ N_t \\ A_t \\ \beta_t \\ 1 \end{pmatrix} + \begin{pmatrix} \eta_{T_m,t} \\ \eta_{T_d,t} \\ 0 \\ \eta_{A,t} \\ \eta_{\beta,t} \\ 0 \end{pmatrix}, \quad (3.6)$$

and  $\boldsymbol{\eta}_t \sim \mathcal{N}(0, \mathbf{Q})$ , where

$$\mathbf{Q} = \begin{pmatrix} \sigma_{\eta,T_m}^2 & 0 & 0 & 0 & 0 & 0 \\ 0 & \sigma_{\eta,T_d}^2 & 0 & 0 & 0 & 0 \\ 0 & 0 & 0 & 0 & 0 & 0 \\ 0 & 0 & 0 & \sigma_{\eta,A}^2 & 0 & 0 \\ 0 & 0 & 0 & 0 & \sigma_{\eta,\beta}^2 & 0 \\ 0 & 0 & 0 & 0 & 0 & 0 \end{pmatrix}. \quad (3.7)$$

The measurement equation  $\mathbf{Y}_t = \mathbf{Z}\mathbf{X}_t + \boldsymbol{\varepsilon}_t$  with multiple data sources is written explicitly as:

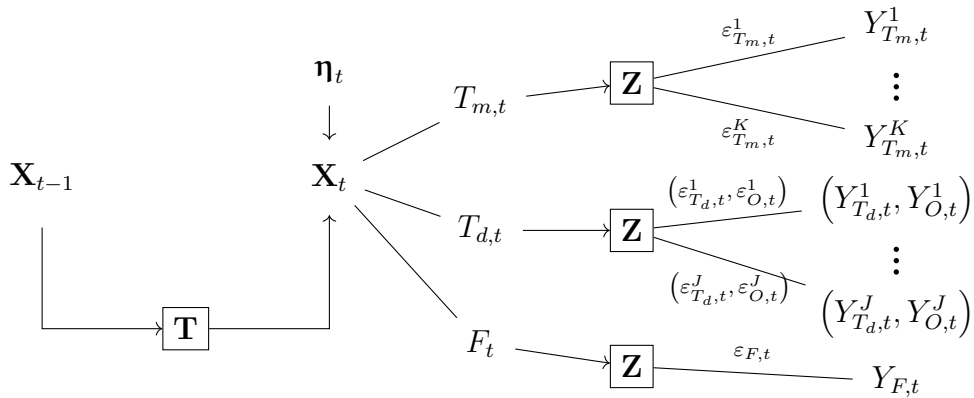
$$\begin{pmatrix} Y_{T_m,t}^1 \\ \vdots \\ Y_{T_m,t}^K \\ Y_{T_d,t}^1 \\ \vdots \\ Y_{T_d,t}^J \\ Y_{O,t}^1 \\ \vdots \\ Y_{O,t}^J \\ Y_{F,t} \end{pmatrix} = \begin{pmatrix} 1 & 0 & 0 & 0 & 0 & 0 \\ \vdots & \vdots & \vdots & \vdots & \vdots & \vdots \\ 1 & 0 & 0 & 0 & 0 & 0 \\ 0 & 1 & 0 & 0 & 0 & 0 \\ \vdots & \vdots & \vdots & \vdots & \vdots & \vdots \\ 0 & 1 & 0 & 0 & 0 & 0 \\ 0 & C_d & 0 & 0 & 0 & 0 \\ \vdots & \vdots & \vdots & \vdots & \vdots & \vdots \\ 0 & C_d & 0 & 0 & 0 & 0 \\ 0 & 0 & 1 & 1 & 0 & 0 \end{pmatrix} \begin{pmatrix} T_{m,t} \\ T_{d,t} \\ N_t \\ A_t \\ \beta_t \\ 1 \end{pmatrix} + \begin{pmatrix} \varepsilon_{T_m,t}^1 \\ \vdots \\ \varepsilon_{T_m,t}^K \\ \varepsilon_{T_d,t}^1 \\ \vdots \\ \varepsilon_{T_d,t}^J \\ \varepsilon_{O,t}^1 \\ \vdots \\ \varepsilon_{O,t}^J \\ \varepsilon_{F,t} \end{pmatrix}, \quad (3.8)$$

and  $\boldsymbol{\varepsilon}_t \sim \mathcal{N}(0, \mathbf{H})$ , where

$$\mathbf{H} = \begin{pmatrix} \sigma_{\varepsilon, Y_{T_m}^1}^2 & 0 & \cdots & 0 & 0 & 0 & \cdots & 0 & 0 & \cdots & 0 & 0 \\ 0 & \sigma_{\varepsilon, Y_{T_m}^2}^2 & \ddots & 0 & 0 & 0 & \cdots & 0 & 0 & \cdots & 0 & 0 \\ \vdots & \ddots & \ddots & \ddots & \vdots & \vdots & \ddots & \vdots & \vdots & \ddots & \vdots & \vdots \\ 0 & 0 & \ddots & \sigma_{\varepsilon, Y_{T_m}^{K-1}}^2 & 0 & 0 & \cdots & 0 & 0 & \cdots & 0 & 0 \\ 0 & 0 & \cdots & 0 & \sigma_{\varepsilon, Y_{T_m}^K}^2 & 0 & \cdots & 0 & 0 & \cdots & 0 & 0 \\ 0 & 0 & \cdots & 0 & 0 & \sigma_{\varepsilon, Y_{T_d}^1}^2 & \ddots & 0 & \rho\sigma_{\varepsilon, Y_{T_d}^1} \sigma_{\varepsilon, Y_O^1} & \ddots & 0 & 0 \\ \vdots & \vdots & \ddots & \vdots & \vdots & \ddots & \ddots & \ddots & \ddots & \ddots & \ddots & \vdots \\ 0 & 0 & \cdots & 0 & 0 & 0 & \ddots & \sigma_{\varepsilon, Y_{T_d}^J}^2 & 0 & \ddots & \rho\sigma_{\varepsilon, Y_{T_d}^J} \sigma_{\varepsilon, Y_O^J} & 0 \\ 0 & 0 & \cdots & 0 & 0 & \rho\sigma_{\varepsilon, Y_{T_d}^1} \sigma_{\varepsilon, Y_O^1} & \ddots & 0 & \sigma_{\varepsilon, Y_O^1}^2 & \ddots & 0 & 0 \\ \vdots & \vdots & \ddots & \vdots & \vdots & \ddots & \ddots & \ddots & \ddots & \ddots & \ddots & \vdots \\ 0 & 0 & \cdots & 0 & 0 & 0 & \ddots & \rho\sigma_{\varepsilon, Y_{T_d}^J} \sigma_{\varepsilon, Y_O^J} & 0 & \ddots & \sigma_{\varepsilon, Y_O^J}^2 & 0 \\ 0 & 0 & \cdots & 0 & 0 & 0 & \cdots & 0 & 0 & \cdots & 0 & \sigma_{\varepsilon, Y_F}^2 \end{pmatrix} \quad (3.9)$$

Since the observation vector  $\mathbf{Y}_t$  contains data measurements of the latent states, the measurement equation matrix  $\mathbf{Z}$  contains 1's on the diagonal with the exception of the equation for OHC, where the heat capacity parameter  $C_d$  enters. When  $K = J = 1$ , the model collapses to the specification with one data source for the latent states. The EBM-SS model with multiple data sources is schematically depicted in Figure 3.4.

Figure 3.4: Diagram of the state space model with multiple data sources, i.e.,  $K$  GMST anomalies,  $J$  pairs of ocean temperature and OHC anomalies, and one forcing as measurements.



## 4 Estimation and simulation of the EBM-SS

The parameters to be estimated in EBM-SS model include the four physical parameters  $\lambda$ ,  $\gamma$ ,  $C_m$ , and  $C_d$ ; the parameters in the variance-covariance matrices of the state disturbances,  $\mathbf{Q}$ , and

of the measurement errors,  $\mathbf{H}$ ; and constants  $\boldsymbol{\mu}_{T_d}$  for the observations of  $T_d$ . These parameters are collected in the parameter vector  $\boldsymbol{\theta}$ . The estimate of  $\boldsymbol{\theta}$  is obtained by maximum likelihood, where the log-likelihood function is evaluated using the Kalman filter, see [Durbin and Koopman \(2012\)](#). We implement the EBM-SS model using the R package KFAS ([Helske, 2017](#)) and optimize the log-likelihood value using a combination of “solnp”<sup>3</sup> ([Ye, 1988](#)) and the Nelder-Mead simplex method ([Nelder & Mead, 1965](#)). For initialization, we adopt the “Big K” technique (illustrated in [Durbin and Koopman \(2012\)](#)) to approximate the diffuse initialization, and we set the initial variances of the non-stationary states as  $10^6$ .

We conduct a Monte Carlo simulation to explore the small-sample properties of the EBM-SS model. We choose a sample size of 66, the length of the historical dataset, and perform 1,000 simulation replications. We consider the EBM-SS base model, where there is one data source for each latent state, and the EBM-SS full model, where there are eight GMST series, two pairs of ocean temperature and OHC series, and one radiative forcing series, all of which are simulated in this exercise. We also allow for correlations between each pair of ocean temperature and OHC. For the EBM-SS full model, we employ the empirical estimates reported in panel A in [Table 6.1](#) as the data-generating parameters to simulate the data. First, we simulate the data for the EBM-SS full model, and we chose the first GMST, first ocean temperature, first OHC, and the radiative forcing series from this set of data as the simulated data for the EBM-SS base model. Hence, these two sets of simulated data share the same source of randomness.

As shown in [Equation \(3.2\)](#), the anthropogenic forcing state  $A_t$  is of integration order 2, as it cumulates a stochastic trend  $\beta_t$ . Simulating the anthropogenic forcing series unrestrictedly inevitably generates trajectories with downward trends, which contradicts the pronounced upward trends observed in the historical series ([Figure 3.2b](#)). To obtain simulated paths that are comparable with the observational records, we apply rejection sampling ([Wells et al., 2004](#)) and only retain the  $i$ th simulated trajectory  $\{Y_{A,t}^{i,\text{sim}}\}_{t=1}^T$ , if it satisfies that:

$$Y_{A,\frac{T}{2}}^{i,\text{sim}} \geq 0.75Y_{A,\frac{T}{2}} \quad \text{and} \quad Y_{A,T}^{i,\text{sim}} \geq 0.75Y_{A,T}, \quad (4.1)$$

where  $Y_{A,\frac{T}{2}}$  and  $Y_{A,T}$  are the mid-point and the endpoint in the historical anthropogenic forcing series from [Hansen et al. \(2011\)](#). This ensures that the simulated trajectories are consistent with the historical series in trending upward.

We calculate equilibrium climate sensitivity (ECS) using the relationship as in, e.g., the IPCC Sixth Assessment Report (AR6) ([Forster et al., 2021](#), Chapter 7):  $\text{ECS} = \frac{F_{2\times\text{CO}_2}}{\lambda}$ , where  $F_{2\times\text{CO}_2}$  is the radiative forcing in response to a doubling of the  $\text{CO}_2$  concentrations in the atmosphere. We use the updated best estimate of  $F_{2\times\text{CO}_2} \approx 3.93$  ( $\pm 0.47$ , 5% – 95% CI)  $\text{W m}^{-2}$  from the IPCC AR6 ([Forster et al., 2021](#), Chapter 7).

[Table 4.1](#) reports data-generating parameter values, estimation biases, standard deviations, root mean squared errors (RMSEs), and mean absolute errors (MAEs) of the simulation exercise.

---

<sup>3</sup>The “solnp” optimizer implements the general nonlinear augmented Lagrange multiplier method.

Table 4.1: Data-generating parameter (DGP) values, estimation biases, standard deviations, and root mean squared errors (RMSEs), and mean absolute errors (MAEs) of the Monte Carlo simulation for the EBM-SS base model and EBM-SS full model. Here,  $\sigma_{\varepsilon, Y_{T_m}^k}^2$ ,  $\sigma_{\varepsilon, Y_{T_d}^j}^2$ , and  $\sigma_{\varepsilon, Y_O^j}^2$  denote the variance of measurement error of the  $k$ th GMST series, of the  $j$ th ocean temperature series, and of the  $j$ th OHC series, respectively.

EBM-SS base model									
	physical parameters					variances of state disturbance			
	$\lambda$	$\gamma$	$C_m$	$C_d$	ECS	$\sigma_{\eta, T_m}^2$	$\sigma_{\eta, T_d}^2$	$\sigma_{\eta, A}^2$	$\sigma_{\eta, \beta}^2$
DGP value	1.0828	1.3027	9.6376	98.4886	3.6294	0.0122	$3.66 \times 10^{-5}$	$4.73 \times 10^{-5}$	$9.72 \times 10^{-6}$
estimation bias	0.0139	0.0308	0.2696	-0.0279	0.1993	-0.0012	$-8.59 \times 10^{-6}$	$-1.82 \times 10^{-5}$	$6.51 \times 10^{-6}$
standard deviation	0.2745	0.2674	2.6176	0.8397	1.0595	0.00354	$3.54 \times 10^{-5}$	$1.72 \times 10^{-5}$	$6.67 \times 10^{-6}$
RMSE	0.2747	0.2691	2.6301	0.8397	1.0776	0.00375	$3.65 \times 10^{-5}$	$2.5 \times 10^{-5}$	$9.32 \times 10^{-6}$
MAE	0.2137	0.2049	1.9236	0.6438	0.7705	0.00295	$2.33 \times 10^{-5}$	$2.03 \times 10^{-5}$	$7.2 \times 10^{-6}$
variances of measurement errors (I)									
	$\sigma_{\varepsilon, Y_{T_m}^1}^2$	$\sigma_{\varepsilon, Y_{T_m}^2}^2$	$\sigma_{\varepsilon, Y_{T_m}^3}^2$	$\sigma_{\varepsilon, Y_{T_m}^4}^2$	$\sigma_{\varepsilon, Y_{T_m}^5}^2$	$\sigma_{\varepsilon, Y_{T_m}^6}^2$	$\sigma_{\varepsilon, Y_{T_m}^7}^2$	$\sigma_{\varepsilon, Y_{T_m}^8}^2$	
DGP value	0.0010								
estimation bias	0.00057								
standard deviation	0.0020								
RMSE	0.0021								
MAE	0.0016								
variances of measurement errors (II)					constant of $T_d$		$\rho_{T_d, O}$		
	$\sigma_{\varepsilon, Y_{T_d}^1}^2$	$\sigma_{\varepsilon, Y_{T_d}^2}^2$	$\sigma_{\varepsilon, Y_O^1}^2$	$\sigma_{\varepsilon, Y_O^2}^2$	$\sigma_{\varepsilon, Y_F}^2$	$\mu_{T_d, 1}$	$\mu_{T_d, 2}$	$\rho_1$	$\rho_2$
DGP value	0.00014		1.5311		$1.61 \times 10^{-11}$	-0.2738		0.9092	
estimation bias	$8.77 \times 10^{-6}$		-1.2819		$5.29 \times 10^{-6}$	-0.0004		-0.0059	
standard deviation	$3.93 \times 10^{-5}$		0.0479		$5.81 \times 10^{-6}$	0.0751		0.1339	
RMSE	$4.03 \times 10^{-5}$		1.2828		$7.85 \times 10^{-6}$	0.0705		0.1339	
MAE	$3.10 \times 10^{-5}$		1.2819		$5.29 \times 10^{-6}$	0.0586		0.0316	

EBM-SS full model									
	physical parameters					variances of state disturbance			
	$\lambda$	$\gamma$	$C_m$	$C_d$	ECS	$\sigma_{\eta, T_m}^2$	$\sigma_{\eta, T_d}^2$	$\sigma_{\eta, A}^2$	$\sigma_{\eta, \beta}^2$
DGP value	1.0828	1.3027	9.6376	98.4886	3.6294	0.0122	$3.66 \times 10^{-5}$	$4.73 \times 10^{-5}$	$9.72 \times 10^{-6}$
estimation bias	0.0309	-0.0205	-0.1332	-0.0021	0.1166	-0.00035	$-3.80 \times 10^{-6}$	$-1.81 \times 10^{-5}$	$6.52 \times 10^{-6}$
standard deviation	0.2686	0.2695	2.2429	0.2052	0.9639	0.00211	$2.54 \times 10^{-5}$	$1.71 \times 10^{-5}$	$6.65 \times 10^{-6}$
RMSE	0.2703	0.2702	2.2458	0.2051	0.9705	0.00214	$2.56 \times 10^{-5}$	$2.49 \times 10^{-5}$	$9.31 \times 10^{-6}$
MAE	0.2093	0.1985	1.7106	0.1587	0.7174	0.00169	$1.55 \times 10^{-5}$	$2.02 \times 10^{-5}$	$7.2 \times 10^{-6}$
variances of measurement errors (I)									
	$\sigma_{\varepsilon, Y_{T_m}^1}^2$	$\sigma_{\varepsilon, Y_{T_m}^2}^2$	$\sigma_{\varepsilon, Y_{T_m}^3}^2$	$\sigma_{\varepsilon, Y_{T_m}^4}^2$	$\sigma_{\varepsilon, Y_{T_m}^5}^2$	$\sigma_{\varepsilon, Y_{T_m}^6}^2$	$\sigma_{\varepsilon, Y_{T_m}^7}^2$	$\sigma_{\varepsilon, Y_{T_m}^8}^2$	
DGP value	0.0010	0.00090	0.00241	0.0118	0.00282	0.00659	0.00074	0.00026	
estimation bias	$-7.18 \times 10^{-6}$	$1.8 \times 10^{-5}$	$-4.65 \times 10^{-6}$	0.00023	$9.68 \times 10^{-5}$	$-6.97 \times 10^{-5}$	$-1.97 \times 10^{-6}$	$-2.44 \times 10^{-6}$	
standard deviation	0.00021	0.00018	0.00045	0.0021	0.00049	0.0012	0.00016	$8.73 \times 10^{-5}$	
RMSE	0.00021	0.00019	0.00045	0.0021	0.00050	0.00115	0.00016	$8.73 \times 10^{-5}$	
MAE	0.00017	0.00015	0.00035	0.00163	0.00040	0.00091	0.00013	$6.97 \times 10^{-5}$	
variances of measurement errors (II)					constant of $T_d$		$\rho_{T_d, O}$		
	$\sigma_{\varepsilon, Y_{T_d}^1}^2$	$\sigma_{\varepsilon, Y_{T_d}^2}^2$	$\sigma_{\varepsilon, Y_O^1}^2$	$\sigma_{\varepsilon, Y_O^2}^2$	$\sigma_{\varepsilon, Y_F}^2$	$\mu_{T_d, 1}$	$\mu_{T_d, 2}$	$\rho_1$	$\rho_2$
DGP value	0.00014	0.00015	1.5311	1.2805	$1.61 \times 10^{-11}$	-0.2738	-0.2802	0.9092	0.9943
estimation bias	$2.41 \times 10^{-6}$	$2.43 \times 10^{-5}$	0.0054	0.2368	$5.29 \times 10^{-6}$	-0.0015	-0.0021	0.0004	0.0007
standard deviation	$2.96 \times 10^{-5}$	$3.49 \times 10^{-5}$	0.3195	0.3129	$5.78 \times 10^{-6}$	0.6907	0.6908	0.0246	0.0016
RMSE	$2.97 \times 10^{-5}$	$4.25 \times 10^{-5}$	0.3194	0.3923	$7.84 \times 10^{-6}$	0.6904	0.6905	0.0246	0.0017
MAE	$2.28 \times 10^{-5}$	$3.35 \times 10^{-5}$	0.2462	0.3111	$5.29 \times 10^{-6}$	0.1099	0.1098	0.019	0.0013

Figure 4.1: Simulated distributions of  $\theta_i - \theta_i^0$  for the five physical parameters from 1,000 Monte Carlo simulations of the EBM-SS base model and the EBM-SS full model. “d” in the titles denotes the difference between the estimate in the simulation and the data-generating value, i.e., the bias. The red, blue, and yellow vertical lines represent the data-generating parameter values, the means, and the medians of the 1,000 estimates from the simulation, respectively.

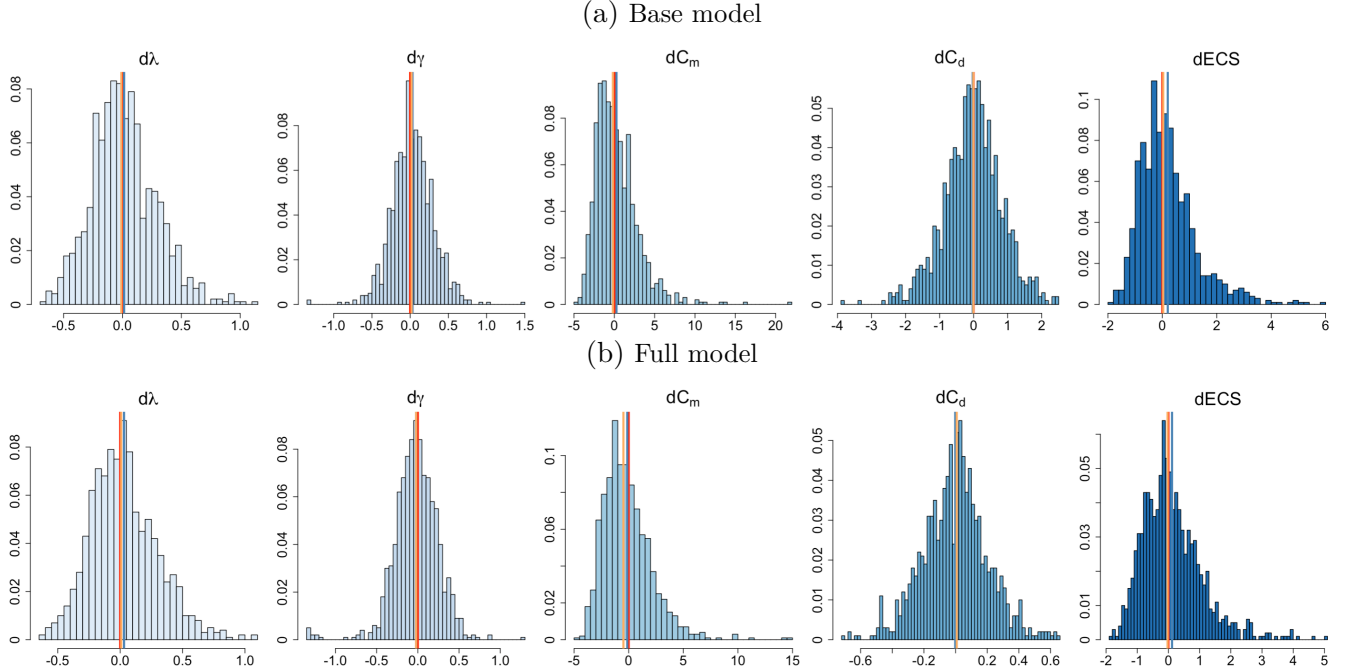


Figure 4.1 shows the distributions of the deviations of the physical parameter estimates in the simulation relative to the true values (denoted as  $d\cdot$ ), which are centered around zero. Among these physical parameters,  $d\gamma$  and  $dC_d$  exhibit the feature of normality, and  $dC_d$  appears much less dispersed for the full model. Under both models,  $d\lambda$  is slightly positive-skewed. Due to the inverse relationship between ECS and  $\lambda$ , the small magnitudes of the estimates of  $\lambda$  produce large ECS estimates, thus the long right tail in  $dECS$ . There are positive skewness and a long right tail in  $dC_m$  as a result of a few large outliers. The small values of the deviations measures in Table 4.1, together with the distributions in Figure 4.1, demonstrate good finite-sample properties of the EBM-SS model.

Comparing the simulation results for the base model and for the full model in Table 4.1, we note that estimation biases, standard deviations, RMSEs, and MAEs decrease, as we include more data series. This provides evidence that including multiple data sources helps decrease the estimation uncertainty.

## 5 Data

This section presents the historical records of anomalies employed in the empirical investigation and the synchronization of these anomalies to a common baseline. For the empirical analysis in this paper, we have collected eight observational GMST datasets from separate research groups,

three pairs of ocean temperature and OHC data series, and one effective radiative forcing series (summarized in Table 5.1) as the measurements for the latent processes in the state equation (3.3) of the EBM-SS model.

Table 5.1: Summary of the anomaly datasets employed in the empirical analysis. The last column “baseline” indicates the reference period or the year upon which the anomalies are constructed.

Variable	Acronym/Type	Institution/Authors	Coverage	Baseline
<b>GMST Anomalies</b>	<a href="#">GISTEMP</a>	NASA	1880 – 2020	1951 – 1980
	<a href="#">NOAAGlobalTemp</a>	NOAA	1880 – 2019	1901 – 2000
	<a href="#">HadCRUT5</a>	Met Office Hadley Center	1850 – 2020	1961 – 1990
	<a href="#">BEST</a>	Berkeley Earth	1850 – 2020	1951 – 1980
	<a href="#">CW14</a>	Cowtan and Way(2014)	1850 – 2020	1961 – 1990
	<a href="#">JMA</a>	Japanese Meteorological Agency	1891 – 2020	1981 – 2010
	<a href="#">ERA-Interim</a>	Copernicus	1970 – 2020	pre-industrial <sup>c</sup>
	<a href="#">JRA-55</a>	Japanese Meteorological Agency	1970 – 2019	pre-industrial <sup>d</sup>
<b>Global Ocean Temperature Anomalies</b>	<a href="#">NOAA yearly, 0-700m</a>	NOAA	1955 – 2020	not specified
	<a href="#">IAP yearly 0-700m, 0-2000m</a>	Institute of Atmospheric Physics	1940 – 2020	1981 – 2010
<b>Global OHC Anomalies</b>	<a href="#">NOAA yearly, 0-700m</a>	NOAA	1955 – 2020	not specified
	<a href="#">IAP yearly 0-700m, 0-2000m</a>	Institute of Atmospheric Physics	1940 – 2020	1981 – 2010
<b>Forcing</b>	<a href="#">Effective Radiative Forcing</a>	Hansen et al. (2011)	1850 – 2018	1850

<sup>c,d</sup> The ERA 5 and JRA 55 yearly series are downloaded from the Copernicus Climate Change Service (C3S) Climate Data Store, which are processed according to [Simmons et al. \(2017\)](#). These two datasets have already been transformed with respect to the pre-industrial period.

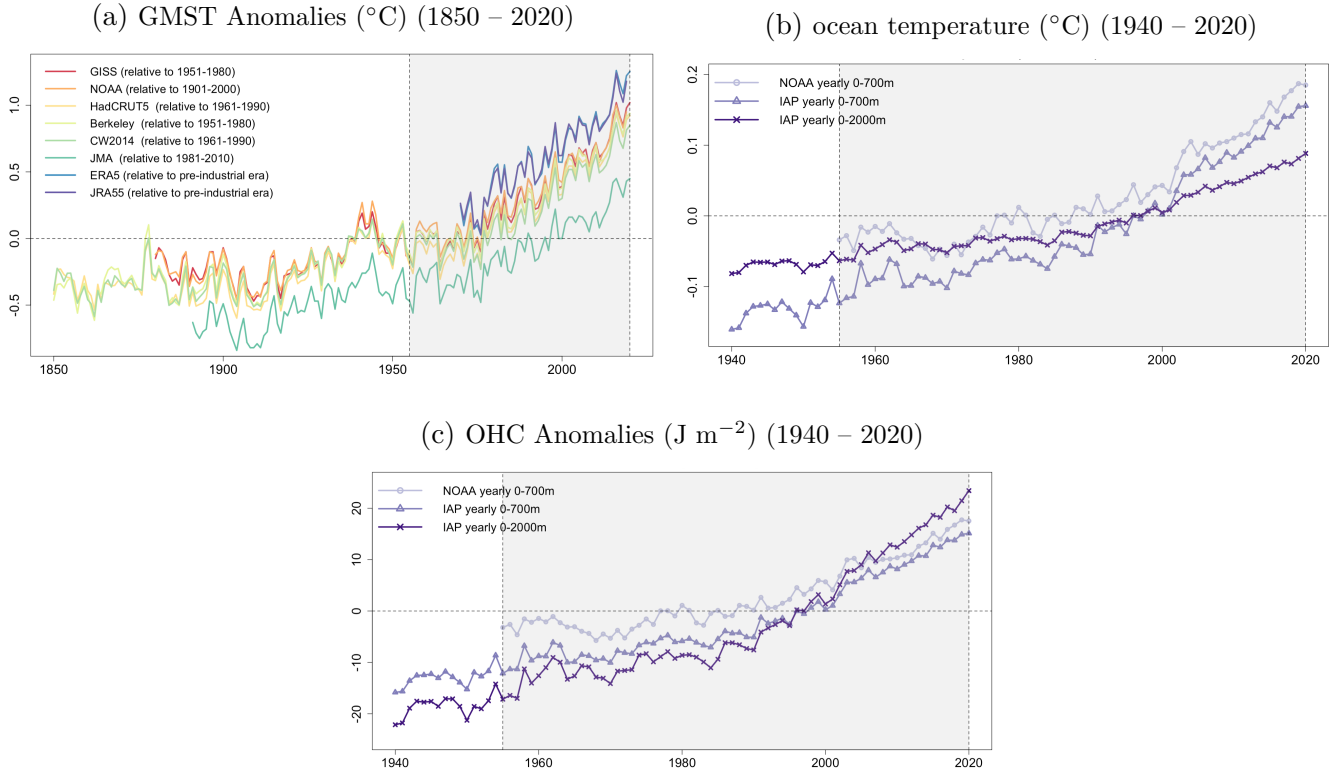
Our choice of the eight GMST datasets is in accordance with that in the IPCC Global Warming of 1.5°C report ([IPCC, 2018](#)), which includes: the GISS Surface Temperature Analysis (GISTEMP) ([GISTEMP Team, 2021](#); [Lenssen et al., 2019](#)), the NOAA Merged Land Ocean Global Surface Temperature Analysis (NOAAGlobalTemp) ([NOAA National Centers for Environmental Information, 2021](#)), HadCRUT5 by the Met Office Hadley Centre ([Morice et al., 2020](#)), the Berkeley Earth Surface Temperatures Land + Ocean (BEST) ([Rohde & Hausfather, 2020](#)), the Cowtan-Way temperature series (CW2014) ([Cowtan & Way, 2014](#)), JMA annual anomalies ([Japan Meteorological Agency, 2021](#)), ERA-Interim reanalysis ([Berrisford et al., 2011](#)), and the Japanese 55-year reanalysis (JRA-55) ([Kobayashi et al., 2015](#)). We assume that each of these datasets represents an independent assessment of the global mean temperature variations.

All of these eight GMST series are in the form of anomalies, i.e., they measure the departures from an average of the observations over a long period (called “reference period” or “baseline”) that usually spans thirty years or longer. It is common practice to record and construct the anomalies rather than the absolute value of the observations ([Hawkins & Sutton, 2016](#)).

Figure 5.1a indicates that, despite having different lengths, these eight GMST series share similar upward trends and fluctuation trajectories, but the ranges they span vary to some extent,



Figure 5.1: GMST, ocean temperature, and OHC anomaly series before synchronization. The light gray area corresponds to the time horizon 1955 – 2020 in the empirical study.



which is mainly due to the different reference periods.

The datasets for the ocean (including both ocean temperature anomalies and OHC anomalies) are from two research bodies, NOAA National Centers for Environment Information (NOAA) and Institute of Atmospheric Physics (IAP), and cover 0-700 and 0-2,000 meter, respectively (see Table 5.1 for details). The OHC anomaly series are estimated based on the in-situ subsurface ocean temperature measurements combined with salinity series (Levitus et al., 2012), and they have the same coverage and baseline as their ocean temperature counterparts. The 0-700m ocean series from NOAA (Levitus et al., 2012) is available since 1955, while the IAP (Cheng et al., 2020) series begins in 1940. As we aim to only use the data based on direct observations, we choose 1955 – 2020 as the time horizon for the empirical study. While the baseline periods for NOAA ocean temperature and OHC anomalies are not documented, IAP benchmarks the ocean series against the 30-year period from 1981 to 2010.

Figure 5.1c shows that all of the OHC series agree on a warming trend but exhibit slightly different yearly variations. According to Von Schuckmann et al. (2020), the global heating rate over the period 1971 – 2018 is estimated as  $0.47 \pm 0.1 \text{ Wm}^{-2}$ , 89% of which is contributed by the global ocean (thereof 52% from the layer 0-700m, 28% from the 700-2,000m, and 9% beyond 2,000m).

We test the stationarity properties of the GMST, ocean temperature, and OHC anomalies, and

we report the results in Table A.2 in Appendix A.1. They indicate that all of these anomaly series are  $I(1)$  processes. As shown in Table A.1, total radiative forcing is also  $I(1)$ , and therefore all of the measurements we consider share the same integration order.

As shown in Table 5.1, the data series have different baselines. The parameter estimates can be distorted if we include several data series with different reference periods simultaneously in a system. Therefore, it is necessary to reconcile these datasets to the same baseline by either synchronizing them before fitting into the model or introducing some structures in the model specification to offset the discrepancies across various baselines. The differences in the baselines across different data sources can be eliminated by synchronizing these anomalies to a common reference period. The simple mathematical arguments for synchronization is given in Appendix A.2.

The pre-industrial era is a natural choice for this common baseline, as it is commonly used as a benchmark to measure and evaluate climate change. We follow the IPCC Global Warming of 1.5°C report (IPCC, 2018) to specify 1850 – 1900 as the pre-industrial base period for GMSTs. The synchronized GMST series are exhibited in Figure A.1a in Appendix A.2. The forcing series we employ in the paper is already benchmarked against 1850. To maintain consistency with the pre-industrial benchmark of GMSTs, we synchronize the anthropogenic forcing as anomalies relative to 1850 – 1900.

It is infeasible to synchronize the ocean series relative to the pre-industrial era, as the ocean information during this period is very sparse. We benchmark the NOAA ocean series against 1981 – 2010 for comparability with IAP series, as shown in Figures A.1b and A.1c in Appendix A.2. What remains to be accommodated is the baseline difference between 1981 – 2010 and the pre-industrial era. A solution we consider here is to introduce a constant  $\mu_{T_d}^j$  to the  $j$ th measurement equation of ocean temperature and to the  $j$ th measurement equation of the corresponding OHC accordingly:

$$\begin{aligned} Y_{T_d,t}^j &= \mu_{T_d}^j + T_{d,t} + \varepsilon_{T_d,t}^j, \\ Y_{O,t}^j &= C_d \mu_{T_d}^j + C_d T_{d,t} + \varepsilon_{O,t}^j, \quad (j = 1, 2, \dots, J). \end{aligned} \tag{5.1}$$

## 6 Empirical results

In this section, we fit the EBM-SS model defined in Section 3 to the datasets described in Section 5. The sample period is 1955 – 2020. The ERA-Interim and JRA-55 GMST anomalies have a shorter length of 51 years, from 1970 to 2020, but the missing observations during 1955 – 1969 are treated in the state space model using the techniques illustrated in Durbin and Koopman (2012).

### 6.1 Parameter estimates by fitting historical observations

Table 6.1 shows the parameter estimates using all of the eight GMST anomalies presented in Section 5. Using the delta method, we account for the uncertainty of the estimates of both  $\lambda$  and  $F_{2 \times \text{CO}_2}$  when calculating the standard error for the ECS estimate, where  $F_{2 \times \text{CO}_2}$  denotes the radiative forcing in response to a doubling of the atmospheric  $\text{CO}_2$  concentrations. The estimation results

with only one data source for each of the latent states are presented in Table A.4 in Appendix A.3.

Of the four physical parameters ( $\lambda$ ,  $\gamma$ ,  $C_m$ , and  $C_d$ ) in the two-component EBM, the estimates

Table 6.1: Parameter estimates from fitting the EBM-SS model to eight synchronized GMST and the radiative forcing series from Hansen et al. (2011). Panel A includes two pairs of ocean temperature and OHC series covering 0-700m from NOAA ( $Y_{T_d}^{\text{NOAA}}, Y_O^{\text{NOAA}}$ ) and IAP ( $Y_{T_d}^{\text{IAP}}, Y_O^{\text{IAP}}$ ). Panel B includes the ocean temperature and OHC series covering 0-2,000m from IAP. All of the GMST anomalies and the ocean series have been synchronized relative to the pre-industrial period and 1981 – 2010, respectively, where the constants for the ocean series offset the baseline difference. The standard errors for estimates are obtained using the delta method and presented in parentheses.  $\hat{\mathbf{H}}$  and  $\hat{\mathbf{Q}}$  denote the estimated variance-covariance matrices of the measurement errors and state disturbances, respectively, and  $\hat{\mathcal{L}}$  denotes the maximized log-likelihood.  $\rho_{\varepsilon_{Y_{T_d}}, \varepsilon_O}^{\text{NOAA}}$  and  $\rho_{\varepsilon_{Y_{T_d}}, \varepsilon_O}^{\text{IAP}}$  denote the correlations between the ocean temperature and OHC series from NOAA and from IAP, respectively.

A. ocean temperature and OHC 0 – 700m from both NOAA and IAP included					
phys. para.	$\hat{\mu}_{Y_{T_d}}$	elements in $\hat{\mathbf{H}}$		diagonal of $\hat{\mathbf{Q}}$	estimated linear relationships
$\hat{\lambda}$ 1.08 (0.25)	$\hat{\mu}_{Y_{T_d}}^{\text{NOAA}}$ -0.27 (0.09)	$\sigma_{\varepsilon, Y_{T_m}}^2$ 0.0003 ~ 0.012 (0.0001) (0.002)	$\sigma_{\eta, T_m}^2$ 0.012 (0.002)		
$\hat{\gamma}$ 1.30 (0.34)	$\hat{\mu}_{Y_{T_d}}^{\text{IAP}}$ -0.28 (0.09)	$\sigma_{\varepsilon, Y_{T_d}}^2$ 0.00014 (0.00005)	$\sigma_{\eta, T_d}^2$ 0.00004 (0.00002)		$T_{m,t} = 0.75 T_{m,t-1} + 0.14 O_{t-1} + 0.10 F_{t-1} + \eta_{T_m,t}$ (0.09) (0.06) (0.03)
$\hat{C}_m$ 9.64 (2.86)		$\sigma_{\varepsilon, Y_{T_d}}^2$ 0.00015 (0.00005)	$\sigma_{\eta, A}^2$ 0.00005 (0.00001)		$T_{d,t} = 0.01 T_{m,t-1} + 0.99 T_{d,t-1} + \eta_{T_d,t}$ (0.003) (0.003)
$\hat{C}_d$ 98.49 (0.26)		$\sigma_{\varepsilon, Y_O}^2$ 1.53 (0.05)	$\sigma_{\eta, \beta}^2$ 0.00001 (0.000006)		
E $\hat{C}_S$ 3.63 (0.89)		$\sigma_{\varepsilon, Y_O}^2$ 1.28 (0.008)			
		$\sigma_{\varepsilon, Y_F}^2$ $1.6 \times 10^{-11}$ ( $1.9 \times 10^{-17}$ )			
		$\rho_{\varepsilon_{Y_{T_d}}, \varepsilon_O}^{\text{NOAA}}$ 0.909 (0.034)			
	$\hat{\mathcal{L}}$ 1240.30	$\rho_{\varepsilon_{Y_{T_d}}, \varepsilon_O}^{\text{IAP}}$ 0.994 (0.002)			
B. ocean temperature and OHC 0 – 2,000m from IAP included					
phys. para.	$\hat{\mu}_{Y_{T_d}}$	elements in $\hat{\mathbf{H}}$		diagonal of $\hat{\mathbf{Q}}$	estimated linear relationships
$\hat{\lambda}$ 0.66 (0.31)	$\hat{\mu}_{Y_{T_d}}^{\text{NOAA}}$ -0.24 (0.09)	$\sigma_{\varepsilon, Y_{T_m}}^2$ 0.0003 ~ 0.012 (0.0001) (0.002)	$\sigma_{\eta, T_m}^2$ 0.012 (0.002)		
$\hat{\gamma}$ 1.82 (0.45)		$\sigma_{\varepsilon, Y_{T_d}}^2$ 0.00001 (0.000006)	$\sigma_{\eta, T_d}^2$ 0.00001 (0.000008)		$T_{m,t} = 0.73 T_{m,t-1} + 0.19 O_{t-1} + 0.11 F_{t-1} + \eta_{T_m,t}$ (0.10) (0.08) (0.03)
$\hat{C}_m$ 9.35 (2.61)		$\sigma_{\varepsilon, Y_O}^2$ 0.70 (0.002)	$\sigma_{\eta, A}^2$ 0.00005 (0.00001)		$T_{d,t} = 0.01 T_{m,t-1} + 0.99 T_{d,t-1} + \eta_{T_d,t}$ (0.002) (0.002)
$\hat{C}_d$ 269.30 (0.42)		$\sigma_{\varepsilon, Y_F}^2$ $3.8 \times 10^{-9}$ ( $7.8 \times 10^{-9}$ )	$\sigma_{\eta, \beta}^2$ 0.00001 (0.000006)		
E $\hat{C}_S$ 5.91 (2.77)	$\hat{\mathcal{L}}$ 1153.51	$\rho_{\varepsilon_{Y_{T_d}}, \varepsilon_O}^{\text{IAP}}$ 0.985 (0.009)			

of the climate feedback parameter  $\lambda$ , of the coefficient of heat transfer  $\gamma$ , and of the heat capacity of the deep ocean layer  $C_d$  show pronounced increases when 0-2,000m ocean data series are employed, which account for more ocean heat uptake. The last column in Table 6.1 reports the estimated two linear relationships specified by the EBM-SS model, i.e., between the state  $T_{m,t}$  and the lag terms of the three latent states  $T_{m,t-1}$ ,  $T_{d,t-1}$ , and  $F_{t-1}$ , and between the state  $T_{d,t}$  and the lag terms  $T_{m,t-1}$  and  $T_{d,t-1}$ . The estimated coefficients are similar regardless of whether ocean 0-700m or 0-2,000m data are employed.

Table 6.2 compares the estimates of the physical parameters from the EBM-SS model with those from other studies. Comparing panel A and panel B reveals that, when fitting the eight

GMST series and 0-700m ocean datasets from NOAA and IAP, our estimates are comparable to those obtained by the CMIP 4×CO<sub>2</sub> experiment data (Cummins et al., 2020; Smith et al., 2021, Chapter 7 supplementary material). Our estimate of the ECS is 3.63°C, which is close to the upper bound of the estimated range of 2.5°C–3.5°C using instrumental records in the IPCC AR6 (Forster et al., 2021, Chapter 7). It is also close to the emergent constrained ECS mean estimates from CMIP5 and CMIP6 (Schlund et al., 2020; Smith et al., 2021, Chapter 7 supplementary material).

Table 6.2: Comparison of estimates for the physical parameters between EBM-SS full model and other studies. The standard errors of the estimates are reported in parentheses, while some standard errors are unavailable. “Chapter 7 SM” represents the supplementary material to Chapter 7 in IPCC AR6.

<b>A. evaluation of the two-component EBM using historical data</b>					
<b>model</b>	$\hat{\lambda}$	$\hat{\gamma}$	$\hat{C}_m$	$\hat{C}_d$	E $\hat{C}$ S
EBM-SS full, 0-700m ocean data (NOAA & IAP)	1.08 (0.25)	1.30 (0.34)	9.64 (2.86)	98.49 (0.26)	3.63 (0.89)
EBM-SS full, 0-2,000m ocean data (IAP)	0.66 (0.31)	1.82 (0.45)	9.35 (2.61)	269.30 (0.42)	5.91 (2.77)
<b>B. evaluation of the two-component EBM using 4×CO<sub>2</sub> experiment data</b>					
<b>model</b>	$\hat{\lambda}$	$\hat{\gamma}$	$\hat{C}_m$	$\hat{C}_d$	E $\hat{C}$ S
CMIP6 means (Smith et al., 2021, Chapter 7 SM)	0.84 (0.38)	0.64 (0.13)	8.1 (1.0)	110 (63)	3.0
CMIP5 means (Cummins et al., 2020)	1.21	0.77	6.88	97.18	3.41
<b>C. estimates of ECS using different datasets and methods</b>					
<b>model and data</b>	$\hat{\lambda}$	$\hat{\gamma}$	$\hat{C}_m$	$\hat{C}_d$	E $\hat{C}$ S
Instrumental records (Forster et al., 2021, Chapter 7)	-	-	-	-	2.5 – 3.5
CMIP6 means (Schlund et al., 2020; Smith et al., 2021)	-	-	-	-	3.78 (1.08)
CMIP5 means (Schlund et al., 2020; Smith et al., 2021)	-	-	-	-	3.28 (0.74)
<b>D. heat capacity by physical relationship</b>					
<b>literature</b>	$C_m$	$C$ at 700m	$C$ at 2000m		
Hartmann (2015)	9.32	93.17	266.2		
Gregory (2000)	14.33	66.85	191		

Panel D in Table 6.2 reports heat capacity values indicated by physical relations. As we employ ocean data covering 0-700m and 0-2,000m in this paper, we also examine the physics-implied heat capacities at these two depths to evaluate the estimation accuracy. Here we have two benchmarks that define different depths for the mixed layer. The first benchmark is by Hartmann (2015), who declares the average depth of the mixed ocean layer that interacts with the atmosphere on a scale of one year is 70 m, and the corresponding heat capacity is 9.32 W year m<sup>-2</sup> K<sup>-14</sup>. Another benchmark considers 150 m as the mean depth (Gregory, 2000) and the heat capacity value for this benchmark is 14.33 W year m<sup>-2</sup> K<sup>-15</sup>. Our estimates of the heat capacities for the mixed layer and deep ocean layer  $C_m$  and  $C_d$  are noticeably close to Hartmann’s benchmarks.

<sup>4</sup>The ocean heat capacity at a specific depth  $d$  is:  $C = d \times 0.1331 \text{WK}^{-1} \text{ m}^{-2} \text{ m}^{-1}$  (Hartmann, 2015).

<sup>5</sup>According to Geoffroy et al. (2013),  $C = d \times 0.0955 \text{WK}^{-1} \text{ m}^{-2} \text{ m}^{-1}$ .

Figure A.2 and Figure A.3 in Appendix A.4 give graphic summaries of the model fit for the EBM-SS full model to two pairs of 0-700m ocean datasets from NOAA and IAP, and to 0-2,000m ocean series from IAP, respectively. These two figures indicate that the smoothed states of the latent states, which are the estimated states given the entire observational trajectory, closely catch the data.

As described in Section 3.4, we assume the state disturbances and measurement errors to be serially uncorrelated and normality distributed. Then, ideally, the standardized one-step ahead prediction errors are also serially uncorrelated and follow a standard normal distribution (Durbin & Koopman, 2012). In Figure A.2 and Figure A.3, the residuals after the fit, the standardized one-step ahead prediction errors, appear centered around zero. Diagnostic statistics of the residuals are reported in Table A.5 in Appendix A.5. The residual series have means close to zero and standard deviations close to one. There is no violation of Gaussianity except for the residuals of ocean temperature 0-2,000m and OHC 0-2,000m from IAP due to the outliers in 1958. There are a few standardized prediction error series showing autocorrelation. This can be attributed to using a single state to fit variations from multiple data series. Overall, the EBM-SS model provides a good fit for the data.

## 6.2 Empirical evidence for estimation uncertainty reduction by using multiple data sources

In Section 4, we have shown in simulations that the multiple-data-source structure in the EBM-SS model is effective in reducing parameter estimation uncertainty. In this section, we examine if the same conclusion can be drawn in the empirical exercise.

In the simulation study, we can directly compare the simulation performances of the EBM-SS base model (single data source) and of the EBM-SS full model (multiple data source). This is because the simulated data for these two models are generated from the same simulations and thus have the same parametrization and randomness. However, the standard errors using different empirical datasets are incomparable due to the varying magnitudes of the mean estimates of the parameters. Therefore, we use the coefficient of variation (CV), defined as the standard error divided by the estimate of the mean, to measure the relative estimation uncertainty.

In Table 6.3, we compare CVs in the EBM-SS base model with those in the EBM-SS full model. Under the EBM-SS base setting, there are sixteen and eight combinations of different series when ocean data 0-700m and ocean data 0-2,000m are employed, respectively. As shown in Table A.4 in Appendix A.3, both the physical parameter estimates and CVs are diverse across the different combinations of series, and thus we use the median of the CVs for the EBM-SS base model.

Table 6.3 shows clearly that the EBM-SS full model with 0-700m and 0-2,000m ocean series produces a lower CV than the medians of CVs for the EBM-SS base model. The last row in Table 6.3 indicates that the majority of individual CVs are equal to or greater than the CV of the EBM-SS full model. One exception is  $\hat{\gamma}$  when IAP 0-2,000m ocean data is employed. Table 6.3 provides

Table 6.3: Comparing coefficients of variation (CVs) of the physical parameters for the EBM-SS full model and the medians of CVs for the EBM-SS base model. CV is calculated as the standard error of the estimate divided by the estimate of the mean. “% CV  $\geq$  \*” reports the percentage where the individual CV of EBM-SS base model is not smaller than the CV of the EBM-SS-full model (denoted as \*).

Setting		NOAA / IAP 0-700m					IAP 0-2,000m				
		$\hat{\lambda}$	$\hat{\gamma}$	$\hat{C}_m$	$\hat{C}_d$	ECS	$\hat{\lambda}$	$\hat{\gamma}$	$\hat{C}_m$	$\hat{C}_d$	ECS
EBM-SS-full	CV (*)	0.23	0.26	0.30	0.003	0.25	0.46	0.25	0.28	0.002	0.47
EBM-SS-base	median of CVs	0.39	0.22	0.37	0.01	0.40	1.20	0.19	0.36	0.002	1.21
	% CV $\geq$ *	93.8%	62.5%	93.8%	50%	93.8%	100%	0	87.5%	100%	100%

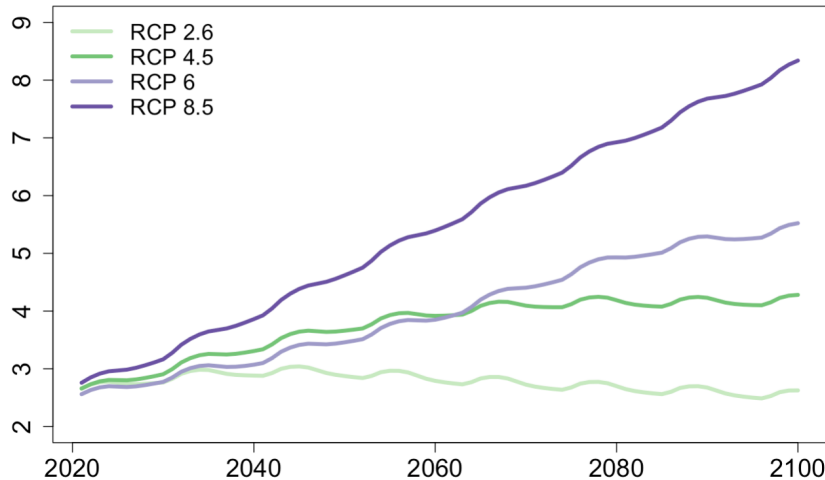
empirical evidence that including multiple data sources reduces the estimation uncertainty.

## 7 Scenario Analysis

In this section, we study long-term projections from the EBM-SS full model using the Representative Concentration Pathway (RCP) scenarios of [Meinshausen, Smith, et al. \(2011\)](#).

RCPs are adopted by [IPCC \(2014\)](#) to represent different possible GHG concentration trajec-

Figure 7.1: Global annual mean radiative forcing ( $\text{Wm}^{-2}$ ) constructed under RCP scenarios ([Meinshausen, Smith, et al., 2011](#)) during 2021 – 2100.



tories in the future until 2100. The four scenarios RCP 2.6, RCP 4.5, RCP 6, and RCP 8.5 denote different levels of radiative forcing values ( $\text{Wm}^{-2}$ ) 2.6, 4.5, 6, and 8.5, respectively, in 2100. The reduced complexity climate model MAGICC6 ([Meinshausen, Raper, & Wigley, 2011](#); [Meinshausen, Wigley, & Raper, 2011](#)) was influential in constructing the RCP pathways. The RCP radiative forcing time series during 2021 – 2100 are shown in Figure 7.1. Except for RCP 2.6, which shows a peak in around 2030 and then decline, the other three pathways are rising over the period. They exhibit cyclical patterns from solar irradiance.

We focus on the projection of GMST for 2021 – 2100 conditional on the RCP forcing series. To take parameter uncertainty into account, we assume that the physical parameter vector follows

a multivariate normal distribution  $\mathcal{N}(\hat{\boldsymbol{\theta}}^*, \hat{\boldsymbol{\Sigma}}^*)$  and draw 10,000 sets of parameters from this distribution, where  $\hat{\boldsymbol{\theta}}^*$  and  $\hat{\boldsymbol{\Sigma}}^*$  denote the estimated mean vector and the estimated variance-covariance matrix of the physical parameter set in the empirical exercise in Table 6.1. We fix the other parameters, such as the variances of measurement errors, at their empirical estimates. We insert each of the parameter sets into the EBM-SS model, which produces point predictions of GMST at  $T + h$  ( $T = 2020$ , and  $h = 1, 2, \dots, 80$ ). We show the median values and the 90% projection confidence intervals in Figure 7.2 under each of the four RCP scenarios.

We produce GMST projections for both the EBM-SS base and the EBM-SS full models. The EBM-SS base model is specified using HadCRUT5 GMST anomalies, together with ocean series (ocean temperature and OHC) from NOAA for 0-700m and from IAP for 0-2,000m. We choose these series because they produce parameter estimates and CVs that are closest to the medians of the values using all combinations of data series (see Table A.4 in Appendix A.3).

In Figure 7.2 and Table 7.1, we compare our GMST projections with the outputs from CMIP5 models and the emulator MAGGIC 7.5, where all of the values are relative to 1850 – 1900. The global scale averaged time series of CMIP5 projections under various RCP scenarios are aggregated by Nicholls et al. (2021). Considering data availability, we include the projection series from 21, 29, 16, and 28 CMIP5 models for RCP 2.6, RCP 4.5, RCP 6.0, and RCP 8.5 scenarios, respectively. The 2081 – 2100 mean results from MAGGIC 7.5 runs use historical observational GHG concentration levels until 2015 and then switch to emission-driven runs (Lee et al., 2021).

Figure 7.2 and Table 7.1 show that our GMST projections produced using the EBM-SS full model and eight GMST historical datasets largely agree with those from CMIP5 models and MAGGIC 7.5. The EBM-SS base model generates both a higher mean projection and a wider confidence band. The wider confidence band is mainly due to the larger estimation uncertainty in the base case. It corroborates the crucial role of multiple data sources in producing more precise projection values. The results are robust to the depth the ocean data (ocean temperature and OHC) covers. Although employing 0-2000m ocean data generates wider confidence bands than using 0-700m, the differences are not large and the medians remain almost unchanged (Table 7.1).

Figure 7.2: Probabilistic projection of GMST during 2021 – 2100 conditional on RCP 2.6, RCP 4.5, RCP 6, and RCP 8.5 forcing series from Meinshausen, Smith, et al. (2011).

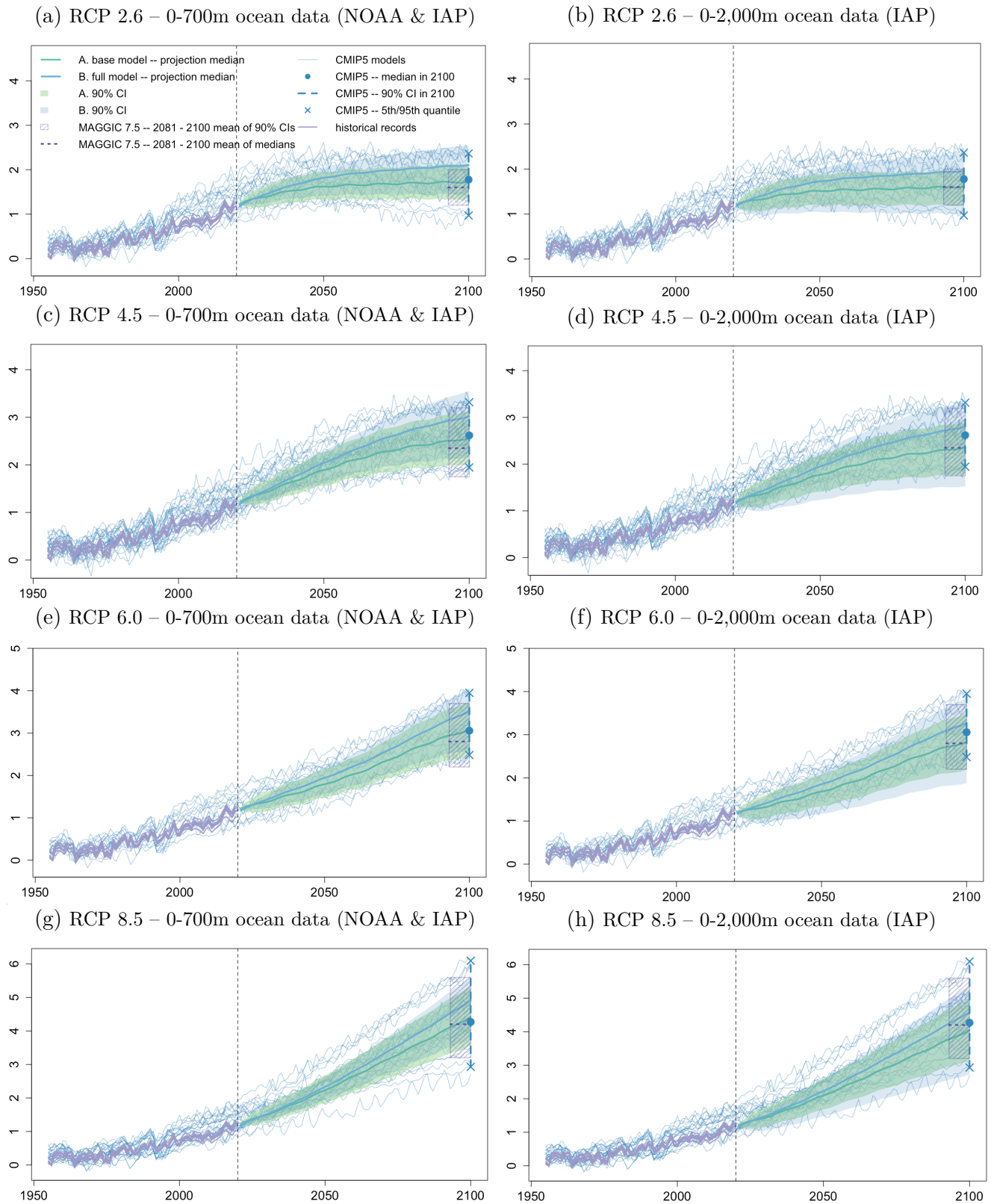




Table 7.1: 5% – 95% ranges and medians of GMST ( $^{\circ}\text{C}$ ) projections in 2100 under RCP scenarios by EBM-SS full model.

		0-700m ocean data (NOAA & IAP)				0-2,000m ocean data (IAP)			
		RCP 2.6	RCP 4.5	RCP 6.0	RCP 8.5	RCP 2.6	RCP 4.5	RCP 6.0	RCP 8.5
<b>Base</b>	median	2.10	3.02	3.51	4.90	1.96	2.81	3.28	4.58
	5% quantile	1.45	2.17	2.63	3.77	0.91	1.39	1.71	2.49
	95% quantile	2.56	3.55	4.05	5.62	2.34	3.34	3.87	5.41
<b>Full</b>	median	1.73	2.57	3.08	4.42	1.61	2.37	2.84	4.06
	5% quantile	1.34	2.02	2.46	3.56	1.21	1.80	2.20	3.17
	95% quantile	2.14	3.14	3.75	5.35	1.97	2.91	3.51	5.02
		MAGGIC 7.5 runs 2081 – 2100 means				CMIP5 outputs			
		RCP 2.6	RCP 4.5	RCP 6.0	RCP 8.5	RCP 2.6	RCP 4.5	RCP 6.0	RCP 8.5
median		1.6	2.35	2.8	4.2	1.78	2.62	3.06	4.27
5% quantile		1.2	1.75	2.2	3.2	0.97	1.95	2.48	2.93
95% quantile		2.0	3.2	3.7	5.6	2.36	3.32	3.95	6.09

## 8 Conclusion

In this paper, we present a statistical climate model (EBM-SS model), which is a multivariate linear Gaussian state space representation of the two-component EBM. The EBM-SS model provides a framework to quantify the temperature change in response to radiative forcing, while taking the thermal inertia of the ocean into account. We incorporate ocean heat content (OHC) as a second measurement of the temperature in the deep ocean, so that the heat capacity for the deep ocean,  $C_d$ , can be constrained using both ocean temperature and OHC historical records.

We incorporate multiple data sources as measurements for the latent states to reduce estimation uncertainty. To account for the different baseline periods in different anomaly series, we synchronize the eight GMST series and the anthropogenic forcing series with respect to the period 1850 – 1900 using the information by [IPCC \(2018\)](#). We include constants for the ocean temperature and OHC series to offset their baseline discrepancies relative to the GMST anomalies and radiative forcing series. Both the empirical and simulation exercises indicate that including eight GMST anomaly series and two pairs of ocean data series as multiple data sources reduces estimation uncertainty of the parameters compared to the models that use only one data source. We obtain physical parameter estimates that are comparable to the ones reported in [Cummins et al. \(2020\)](#) and [Smith et al. \(2021, Chapter 7 SM\)](#).

We show that fitting the EBM-SS model to a comprehensive data set of GMST anomalies, ocean temperature, and OHC over the period 1955 – 2020 from separate research groups produces projections for GMSTs that are comparable to those of CMIP5 ([Nicholls et al., 2021](#)) and MAG-ICC 7.5 ([Lee et al., 2021](#)) for RCP 2.6, RCP 4.5, and RCP 6. Our results thus corroborate earlier findings from both complex climate models and reduced-complexity models, where our statistical

model exclusively uses historical data. Our model is, in contrast to earlier models, a small-scale statistical model that can be estimated using standard software packages on standard office computers. Its statistical nature allows for the assessment of parameter uncertainty.

## References

- Berrisford, P., Dee, D., Poli, P., Brugge, R., Fielding, M., Fuentes, M., . . . Simmons, A. (2011, 11). The ERA-Interim archive version 2.0. (1), 23. Retrieved from <https://www.ecmwf.int/node/8174>
- Budyko, M. I. (1969). The effect of solar radiation variations on the climate of the Earth. *Tellus*, 21(5), 611–619.
- Caines, P. E. (1988). *Linear stochastic systems*. John Wiley & Sons.
- Castle, J., & Hendry, D. (2019). *Modelling our changing world*. Springer Nature.
- Castle, J., & Hendry, D. F. (2020). Climate econometrics: An overview. *Foundations and Trends in Econometrics*, 10(3-4).
- Chang, Y., Kaufmann, R. K., Kim, C. S., Miller, J. I., Park, J. Y., & Park, S. (2020). Evaluating trends in time series of distributions: A spatial fingerprint of human effects on climate. *Journal of Econometrics*, 214(1), 274–294.
- Cheng, L., Trenberth, K. E., Gruber, N., Abraham, J. P., Fasullo, J. T., Li, G., . . . Zhu, J. (2020). Improved estimates of changes in upper ocean salinity and the hydrological cycle. *Journal of Climate*, 33(23), 10357–10381.
- Colman, R., & Soldatenko, S. (2020). Understanding the links between climate feedbacks, variability and change using a two-layer energy balance model. *Climate Dynamics*, 54(7), 3441–3459.
- Cowtan, K., & Way, R. G. (2014). Coverage bias in the HadCRUT4 temperature series and its impact on recent temperature trends. *Quarterly Journal of the Royal Meteorological Society*, 140(683), 1935–1944.
- Cox, D. C., & Baybutt, P. (1981). Methods for uncertainty analysis: a comparative survey. *Risk Analysis*, 1(4), 251–258.
- Cummins, D. P., Stephenson, D. B., & Stott, P. A. (2020). Optimal estimation of stochastic energy balance model parameters. *Journal of Climate*, 33(18), 7909–7926.
- Dickey, D. A., & Fuller, W. A. (1979). Distribution of the estimators for autoregressive time series with a unit root. *Journal of the American Statistical Association*, 74(366a), 427–431.
- Dijkstra, H. A. (2008). *Dynamical oceanography* (1st ed.). Springer-Verlag Berlin Heidelberg.
- Durbin, J., & Koopman, S. J. (2012). *Time series analysis by state space methods* (Revised ed.). Oxford University Press.
- Forster, P., Storelvmo, T., Armour, K., Collins, W., Dufresne, J.-L., Frame, D., . . . Zhang, H. (2021). The Earth’s energy budget, climate feedbacks, and climate sensitivity. In V. Masson-Delmotte et al. (Eds.), *Climate change 2021: The physical science basis. Contribution of Working Group I to the sixth assessment report of the Intergovernmental Panel on Climate Change*. Cambridge: Cambridge University Press. In Press.
- Geoffroy, O., Saint-Martin, D., Olivié, D. J., Voldoire, A., Bellon, G., & Tytéca, S. (2013). Transient climate response in a two-layer energy-balance model. Part I: Analytical solution and parameter calibration using CMIP5 AOGCM experiments. *Journal of Climate*, 26(6),

1841–1857.

- Gillingham, K., Nordhaus, W., Anthoff, D., Blanford, G., Bosetti, V., Christensen, P., . . . Reilly, J. (2018). [Modeling uncertainty in integrated assessment of climate change: A multimodel comparison](#). *Journal of the Association of Environmental and Resource Economists*, 5(4), 791–826.
- GISTEMP Team. (2021). *GISS Surface Temperature Analysis (GISTEMP), version 4*. NASA Goddard Institute for Space Studies. (Data retrieved from <https://data.giss.nasa.gov/gistemp/>)
- Granger, C. W., & Newbold, P. (1974). [Spurious regressions in econometrics](#). *Journal of Econometrics*, 2(2), 111–120.
- Gregory, J. M. (2000). [Vertical heat transports in the ocean and their effect on time-dependent climate change](#). *Climate Dynamics*, 16(7), 501–515.
- Hansen, J., Sato, M., Kharecha, P., & von Schuckmann, K. (2011). [Earth’s energy imbalance and implications](#). *Atmospheric Chemistry and Physics*, 11, 13421–13449.
- Hartmann, D. L. (2015). *Global physical climatology* (2nd ed.). Elsevier Science.
- Hasselmann, K., Sausen, R., Maier-Reimer, E., & Voss, R. (1993). [On the cold start problem in transient simulations with coupled atmosphere-ocean models](#). *Climate Dynamics*, 9(2), 53–61.
- Hawkins, E., & Sutton, R. (2016). [Connecting climate model projections of global temperature change with the real world](#). *Bulletin of the American Meteorological Society*, 97(6), 963–980.
- Held, I. M., Winton, M., Takahashi, K., Delworth, T., Zeng, F., & Vallis, G. K. (2010). [Probing the fast and slow components of global warming by returning abruptly to preindustrial forcing](#). *Journal of Climate*, 23(9), 2418–2427.
- Helske, J. (2017). [KFAS: Exponential family state space models in R](#). *Journal of Statistical Software*, 78(10).
- Imkeller, P. (2001). [Energy balance models – viewed from stochastic dynamics](#). In Imkeller, P and Storch, J.-S. (Ed.), *Stochastic Climate Models* (pp. 213–240). Springer.
- IPCC. (2014). *Climate change 2014: Synthesis report. Contribution of Working Groups I, II and III to the fifth assessment report of the Intergovernmental Panel on Climate Change*. IPCC, Geneva, Switzerland.
- IPCC. (2018). *Global Warming of 1.5 °C: An IPCC Special Report on the impacts of global warming of 1.5 °C above pre-industrial levels and related global greenhouse gas emission pathways, in the context of strengthening the global response to the threat of climate change, sustainable development, and efforts to eradicate poverty* (V. Masson-Delmotte et al., Eds.). Cambridge: Cambridge University Press. In Press.
- Japan Meteorological Agency. (2021). *Annual Anomalies of Global Average Surface Temperature*. (Data retrieved on 23 June, 2021 from [https://ds.data.jma.go.jp/tcc/tcc/products/gwp/temp/list/year\\_wld.html](https://ds.data.jma.go.jp/tcc/tcc/products/gwp/temp/list/year_wld.html))
- Jarque, C. M., & Bera, A. K. (1980). [Efficient tests for normality, homoscedasticity and serial](#)

- independence of regression residuals. *Economics Letters*, 6(3), 255–259.
- Jiménez-de-la Cuesta, D., & Mauritsen, T. (2019). Emergent constraints on Earth’s transient and equilibrium response to doubled CO<sub>2</sub> from post-1970s global warming. *Nature Geoscience*, 12(11), 902–905.
- Jonko, A., Urban, N. M., & Nadiga, B. (2018). Towards Bayesian hierarchical inference of equilibrium climate sensitivity from a combination of CMIP5 climate models and observational data. *Climatic Change*, 149(2), 247–260.
- Kaufmann, R. K., Kauppi, H., Mann, M. L., & Stock, J. H. (2013). Does temperature contain a stochastic trend: Linking statistical results to physical mechanisms. *Climatic Change*, 118(3-4), 729–743.
- Kim, S.-Y., Huh, D., Zhou, Z., & Mun, E.-Y. (2020). A comparison of Bayesian to maximum likelihood estimation for latent growth models in the presence of a binary outcome. *International Journal of Behavioral Development*, 44(5), 447–457.
- Kobayashi, S., Ota, Y., Harada, Y., Ebata, A., Moriya, M., Onoda, H., . . . others (2015). The JRA-55 reanalysis: General specifications and basic characteristics. *Journal of the Meteorological Society of Japan. Ser. II*, 93(1), 5–48.
- Koll, D. D. B., & Cronin, T. W. (2018). Earth’s outgoing longwave radiation linear due to H<sub>2</sub>O greenhouse effect. *Proceedings of the National Academy of Sciences of the United States of America*, 115(41), 10293–10298.
- Lee, J. Y., Marotzke, J., Bala, G., Cao, L., Corti, S., Dunne, J. P., . . . Zhou, T. (2021). Future global climate: scenario-based projections and near-term information. In V. Masson-Delmotte et al. (Eds.), *Climate change 2021: The physical science basis. Contribution of Working Group I to the sixth assessment report of the Intergovernmental Panel on Climate Change*. Cambridge: Cambridge University Press. In Press.
- Lenssen, N. J., Schmidt, G. A., Hansen, J. E., Menne, M. J., Persin, A., Ruedy, R., & Zyss, D. (2019). Improvements in the GISTEMP uncertainty model. *Journal of Geophysical Research: Atmospheres*, 124(12), 6307–6326.
- Levitus, S., Antonov, J. I., Boyer, T. P., Baranova, O. K., Garcia, H. E., Locarnini, R. A., . . . others (2012). World ocean heat content and thermosteric sea level change (0–2000m), 1955–2010. *Geophysical Research Letters*, 39(10).
- Ljung, G. M., & Box, G. E. (1978). On a measure of lack of fit in time series models. *Biometrika*, 65(2), 297–303.
- Meinshausen, M., Raper, S. C., & Wigley, T. M. (2011). Emulating coupled atmosphere-ocean and carbon cycle models with a simpler model, MAGICC6–Part 1: Model description and calibration. *Atmospheric Chemistry and Physics*, 11(4), 1417–1456.
- Meinshausen, M., Smith, S. J., Calvin, K., Daniel, J. S., Kainuma, M. L., Lamarque, J.-F., . . . others (2011). The RCP greenhouse gas concentrations and their extensions from 1765 to 2300. *Climatic Change*, 109(1), 213–241.
- Meinshausen, M., Wigley, T., & Raper, S. (2011). Emulating atmosphere-ocean and carbon cycle

- models with a simpler model, MAGICC6–Part 2: Applications. *Atmospheric Chemistry and Physics*, 11(4), 1457–1471.
- Morice, C. P., Kennedy, J. J., Rayner, N. A., Winn, J., Hogan, E., Killick, R., ... Simpson, I. (2020). An updated assessment of near-surface temperature change from 1850: The HadCRUT5 dataset. *Journal of Geophysical Research: Atmospheres*.
- Myhre, G., Shindell, D., Bréon, F.-M., Collins, W., Fuglestedt, J., Huang, J., ... Zhang, H. (2013). Anthropogenic and natural radiative forcing. In T. F. Stocker et al. (Eds.), *Climate change 2013: The physical science basis. Contribution of Working Group I to the fifth assessment report of the Intergovernmental Panel on Climate Change* (pp. 659–740). Cambridge, UK: Cambridge University Press.
- Nelder, J. A., & Mead, R. (1965). A simplex method for function minimization. *The Computer Journal*, 7(4), 308–313.
- Nicholls, Z., Lewis, J., Makin, M., Nattala, U., Zhang, G. Z., Mutch, S. J., ... Meinshausen, M. (2021). Regionally aggregated, stitched and de-drifted CMIP-climate data, processed with netCDF-SCM v2.0.0. *Geoscience Data Journal*, 8(2), 154–198.
- Nijssen, F. J., Cox, P. M., & Williamson, M. S. (2020). Emergent constraints on transient climate response (TCR) and equilibrium climate sensitivity (ECS) from historical warming in CMIP5 and CMIP6 models. *Earth System Dynamics*, 11(3), 737–750.
- NOAA National Centers for Environmental Information. (2021). Climate at a glance: Global time series.  
(published June 2021, retrieved on June 23, 2021 <https://www.ncdc.noaa.gov/cag/>)
- North, G. R., Cahalan, R. F., & Coakley Jr, J. A. (1981). Energy balance climate models. *Reviews of Geophysics*, 19(1), 91–121.
- Paltridge, G. W. (1981). Thermodynamic dissipation and the global climate system. *Quarterly Journal of the Royal Meteorological Society*, 107(453), 531–547.
- Pretis, F. (2020). Econometric modelling of climate systems: The equivalence of energy balance models and cointegrated vector autoregressions. *Journal of Econometrics*, 214(1), 256–273.
- Raynaud, D., Jouzel, J., Barnola, J., Chappellaz, J., Delmas, R., & Lorius, C. (1993). The ice record of greenhouse gases. *Science*, 926–934.
- Reyer, C. P., Flechsig, M., Lasch-Born, P., & Van Oijen, M. (2016). Integrating parameter uncertainty of a process-based model in assessments of climate change effects on forest productivity. *Climatic Change*, 137(3), 395–409.
- Rohde, R. A., & Hausfather, Z. (2020). The Berkeley Earth land/ocean temperature record. *Earth System Science Data*, 12(4), 3469–3479.
- Schlund, M., Lauer, A., Gentine, P., Sherwood, S. C., & Eyring, V. (2020). Emergent constraints on equilibrium climate sensitivity in CMIP5: Do they hold for CMIP6? *Earth System Dynamics*, 11(4), 1233–1258.
- Schwartz, S. E. (2007). Heat capacity, time constant, and sensitivity of Earth’s climate system. *Journal of Geophysical Research: Atmospheres*, 112(D24).

- Schwarz, G. (1978). [Estimating the dimension of a model](#). *The Annals of Statistics*, 461–464.
- Sellers, W. D. (1969). [A global climatic model based on the energy balance of the earth-atmosphere system](#). *Journal of Applied Meteorology*, 8(3), 392–400.
- Simmons, A., Berrisford, P., Dee, D., Hersbach, H., Hirahara, S., & Thépaut, J.-N. (2017). [A reassessment of temperature variations and trends from global reanalyses and monthly surface climatological datasets](#). *Quarterly Journal of the Royal Meteorological Society*, 143(702), 101–119.
- Smith, C., Forster, P. M., Allen, M., Leach, N., Millar, R. J., Passerello, G. A., & Regayre, L. A. (2018). [FAIR v1.3: a simple emissions-based impulse response and carbon cycle model](#). *Geoscientific Model Development*, 11(6), 2273–2297.
- Smith, C., Nicholls, Z., Armour, K., Collins, W., Forster, P., Meinshausen, M., . . . Watanabe, M. (2021). [The Earth’s energy budget, climate feedbacks, and climate sensitivity supplementary material](#). In V. Masson-Delmotte et al. (Eds.), *Climate change 2021: The physical science basis. Contribution of Working Group I to the sixth assessment report of the Intergovernmental Panel on Climate Change*. Cambridge: Cambridge University Press. In Press.
- Soldatenko, S., & Colman, R. (2019). [Climate variability from annual to multi-decadal timescales in a two-layer stochastic energy balance model: analytic solutions and implications for general circulation models](#). *Tellus A: Dynamic Meteorology and Oceanography*, 71(1).
- Von Schuckmann, K., Cheng, L., Palmer, M. D., Hansen, J., Tassone, C., Aich, V., . . . others (2020). [Heat stored in the Earth system: Where does the energy go?](#) *Earth System Science Data*, 12(3), 2013–2041.
- Wells, M. T., Casella, G., Robert, C. P., et al. (2004). [Generalized accept-reject sampling schemes](#). In *A festschrift for herman rubin* (Vol. 45, pp. 342–348). Institute of Mathematical Statistics.
- Winsberg, E. (2012). [Values and uncertainties in the predictions of global climate models](#). *Kennedy Institute of Ethics Journal*, 22(2), 111–137.
- Ye, Y. (1988). [Interior algorithms for linear, quadratic, and linearly constrained convex programming](#) (PhD dissertation). Stanford University.
- Young, P. C., Ng, C. N., Lane, K., & Parker, D. (1991). [Recursive forecasting, smoothing and seasonal adjustment of non-stationary environmental data](#). *Journal of Forecasting*, 10(1-2), 57–89.

# A Appendix

## A.1 Unit root tests on the historical data

Table A.1: Augmented Dickey-Fuller (ADF) test (Dickey & Fuller, 1979) for unit roots on level and first-order difference of the observational series for different components of anthropogenic forcing, total anthropogenic forcing  $Y_{A,t}$ , and total forcing  $Y_{F,t}$  during 1955 – 2018. The null hypothesis of the ADF test is the existence of a unit root, i.e., non-stationarity. "f + greenhouse gas name" indicates the forcing from a specific greenhouse gas. \*\* and \* mark significance at 1 % and 5 %, respectively. We report the test statistics when lag order  $k$  equals to 0, 1, 2, and 3, respectively. The values in bold indicate the optimal lag order selected by Bayesian information criterion (BIC) (Schwarz, 1978). The maximum order of lags considered is 15.

Lag order $k$	Level series with constant				First-order difference							
					(a). with constant <sup>a</sup>				(b). with constant and trend			
	0	1	2	3	0	1	2	3	0	1	2	3
fCO <sub>2</sub>	<b>7.43</b>	4.64	4.28	3.42	<b>-4.42**</b>	-3.23*	-2.19	-1.68	<b>-7.19**</b>	-5.93**	-4.41**	-3.85*
fCH <sub>4</sub>	-6.90**	<b>-2.54</b>	-2.41	-2.30	<b>-1.83</b>	-1.68	-1.10	-0.99	<b>-2.94</b>	-2.73	-2.00	-1.84
fCFCs	-2.73	<b>-2.13</b>	-2.24	-2.18	-1.19	<b>-0.93</b>	-1.23	-1.24	<b>-1.76</b>	-1.52	-1.85	-1.83
fN <sub>2</sub> O	<b>4.91</b>	5.11	3.96	3.18	<b>-6.97**</b>	-3.72**	-2.66	-1.92	<b>-10.16**</b>	-6.11**	-4.62**	-3.28
fO <sub>3</sub>	<b>-5.62**</b>	-4.25**	-2.47	-2.09	-4.58**	<b>-2.13</b>	-1.58	-1.39	-5.98**	<b>-2.67</b>	-1.89	-1.68
fTA+SA	-9.09**	<b>-2.34</b>	-2.04	-2.18	<b>-1.60</b>	-1.26	-1.13	-1.35	<b>-2.77</b>	-2.27	-2.28	-2.29
fWMGHGs	2.16	<b>0.79</b>	0.43	0.09	<b>-4.28**</b>	-3.27*	-2.59	-2.09	<b>-4.36**</b>	-3.27**	-2.53	-2.03
$Y_{A,t}$	3.67	<b>1.69</b>	1.18	0.76	<b>-4.41**</b>	-3.25*	-2.61	-2.19	<b>-4.89**</b>	-3.53*	-2.73	-2.25
$Y_{F,t}$	-2.29	-2.91	<b>-1.72</b>	-1.56	-6.01**	<b>-6.92**</b>	-5.16**	-4.64**	-5.96**	<b>-6.90**</b>	-5.17**	-4.69**

<sup>a</sup> ADF test regression with constant:  $\Delta y_t = \alpha + \pi y_{t-1} + \sum_{j=1}^k \gamma_j \Delta y_{t-j} + \varepsilon_t$ . Under the null hypothesis  $\pi = 0$ , the regression equation is reduced to a random walk process with drift.

<sup>b</sup> ADF test regression with constant and trend:  $\Delta y_t = \alpha + \beta t + \pi y_{t-1} + \sum_{j=1}^k \gamma_j \Delta y_{t-j} + \varepsilon_t$ .



Table A.2: ADF test for unit roots on level and first-order difference series of different GMST, ocean temperature, and OHC anomalies during 1955 – 2020. \*\* and \* denote significance at 1% and 5%. As in Table A.1, we conduct the tests with constant alone or both constant and trend included (the explicit expressions are reported in the footnote for Table A.1). Subtable (a) reports the test statistics for each of these specifications examined under lag order 0, 1, 2, and 3. The values in bold indicate the optimal lag orders selected by Bayesian information criterion (BIC). The maximum order of lags considered is 15. Subtable (b) reports the optimal lag orders and test statistics for NOAA OHC 0-700m, IAP OHC 0-700m, and IAP OHC 0-2,000m, where the optimal lag orders exceed 3.

(a)

Lag order $k$	Level series				First-order difference							
	(1). with constant				(2). with constant <sup>a</sup>				(3). with constant and trend			
	0	1	2	3	0	1	2	3	0	1	2	3
GISTEMP	-0.99	-0.53	<b>0.26</b>	0.83	-11.05**	<b>-8.80**</b>	-7.64**	-4.68**	-10.99**	<b>-8.85**</b>	-7.84**	-4.94**
NOAAGlobalTemp	-1.27	-0.95	<b>-0.07</b>	0.59	-10.59**	<b>-8.86**</b>	-7.50**	-4.70**	-10.51**	<b>-8.85**</b>	-7.64**	-4.91**
HadCRUT5	-1.07	-0.57	<b>0.15</b>	0.70	-11.36**	<b>-8.89**</b>	-7.70**	-4.78**	-11.30**	<b>-8.93**</b>	-7.88**	-5.00**
BEST	-1.17	-0.61	<b>0.16</b>	0.76	-11.53**	<b>-9.02**</b>	-7.88**	-4.83**	-11.47**	-9.06**	<b>-8.09**</b>	-5.08**
CW2014	-1.22	-0.66	<b>0.12</b>	0.69	-11.32**	<b>-9.07**</b>	-7.82**	-4.88**	-11.26**	-9.11**	<b>-8.02**</b>	-5.15**
JMA	-1.59	-1.30	<b>-0.37</b>	0.24	-10.45**	<b>-8.77**</b>	-7.76**	-4.73**	-10.37**	-8.73**	<b>-7.83**</b>	-4.84**
ERA-Interim	<b>-1.12</b>	-0.85	-0.29	0.02	-9.39**	<b>-7.69**</b>	-5.75**	-4.18**	-9.30**	<b>-7.64**</b>	-5.77**	-4.12*
JRA-55	<b>-1.22</b>	-0.94	-0.36	0.08	-9.47**	<b>-7.82**</b>	-6.01**	-4.26**	-9.37**	<b>-7.76**</b>	-6.04**	-4.19**
NOAA Ocean Temp <sub>0-700m</sub>	<b>0.49</b>	1.39	1.52	1.99	<b>-10.97**</b>	-6.98**	-5.35**	-3.05*	<b>-11.50**</b>	-7.47**	-6.29**	-3.81*
IAP Ocean Temp <sub>0-700m</sub>	<b>0.24</b>	0.81	1.19	2.35	<b>-10.46**</b>	-7.51**	-6.52**	-4.66**	<b>-10.60**</b>	-7.77**	-7.48**	-5.52**
IAP Ocean Temp <sub>0-2,000m</sub>	<b>0.91</b>	1.27	1.58	2.62	<b>-9.28**</b>	-7.05**	-5.78**	-4.24**	<b>-9.56**</b>	-7.43**	-6.85**	-5.16**
NOAA OHC <sub>0-700m</sub>	0.40	1.19	1.56	2.02	-10.75**	-7.61**	-5.61**	<b>-3.11*</b>	-11.19**	-8.11**	-6.56**	-3.86*
IAP OHC <sub>0-700m</sub>	0.24	0.87	1.26	2.38	-10.80**	-7.69**	-6.45**	-4.60**	-10.96**	-7.97**	-7.44**	-5.51**
IAP OHC <sub>0-2,000m</sub>	0.84	1.24	1.52	2.53	-9.45**	-7.14**	-5.76**	-4.24**	-9.72**	-7.50**	-6.78**	-5.12**

(b)

	Level series		First-order difference			
	(1). with constant		(2). with constant		(3). with constant and trend	
	optimal lag order	t-stat	optimal lag order	t-stat	optimal lag order	t-stat
NOAA OHC <sub>0-700m</sub>	14	2.46			13	-4.00**
IAP OHC <sub>0-700m</sub>	10	1.87	9	-2.52	10	-3.61*
IAP OHC <sub>0-2,000m</sub>	10	1.92	13	-1.22	10	-3.61*

## A.2 Synchronizing anomalies to a common baseline

We show that we can directly synchronize anomaly series of different reference periods to a common baseline. Take a yearly global-level anomaly series  $\{T_t^{\text{anom},1}\}_{t=1}^T$  such that  $T_t^{\text{anom},1} = f(T_{j,\tau}^{\text{grid}} - \bar{T}_j^{\text{ref1}})$ , where  $T_{j,\tau}^{\text{grid}}$  is the raw gridded temperature level at time  $\tau$  and location  $j$ ,  $\tau$  is the time index at higher frequency than a year, and  $\bar{T}_j^{\text{ref1}}$  is the average of the temperatures at location  $j$  over a pre-defined reference period ref1.  $f(\cdot)$  is the linear operator that integrates high-resolution data into a yearly global value. Suppose we would like to get the anomalies over another reference period ref2, e.g., 1981-2010. Using linearity of  $f(\cdot)$ , the new anomaly  $T_t^{\text{anom},2}$  at time  $t$  can be obtained by:

$$\begin{aligned}
 T_t^{\text{anom},2} &= f(T_{j,\tau}^{\text{grid}} - \bar{T}_j^{\text{ref2}}) \\
 &= f(T_{j,\tau}^{\text{grid}}) - f(\bar{T}_j^{\text{ref2}}) + f(\bar{T}_j^{\text{ref1}}) - f(\bar{T}_j^{\text{ref1}}) \\
 &= f(T_{j,\tau}^{\text{grid}} - \bar{T}_j^{\text{ref1}}) - (f(\bar{T}_j^{\text{ref2}}) - f(\bar{T}_j^{\text{ref1}})) \\
 &= T_t^{\text{anom},1} - (\bar{T}^{\text{ref2}} - \bar{T}^{\text{ref1}}),
 \end{aligned} \tag{A.1}$$

where  $\bar{T}^{\text{ref2}} - \bar{T}^{\text{ref1}}$  is the difference between the two average global yearly temperatures over the two reference periods ref1 and ref2. Then we can synchronize the anomalies to ref2 by subtracting  $\bar{T}^{\text{ref2}} - \bar{T}^{\text{ref1}}$  from the original anomalies.

We use Equation (A.1) and the information in the IPCC report 1.5°C report (IPCC, 2018) to get the average GMST values during the pre-industrial era,  $\bar{T}^{\text{pre-ind}}$ , for each of the data sources. The results are reported in Table A.3. The downloaded ERA-Interim and JRA-55 datasets are already transformed relative to the pre-industrial level using the same method as in this paper, and hence we leave them as they are. We subtract  $\bar{T}^{\text{pre-ind}}$  from other GMST series to get the synchronized series.

Table A.3: Averages of the GMST series over 1986 – 2005  $\bar{T}_i^{1986-2005}$ , changes of the averages over 1986 – 2005 relative to the pre-industrial era (1850 – 1900)  $\Delta T_{\text{pre-ind}}^{1986-2005}$ , and averages over 1850 – 1900  $\bar{T}_i^{\text{pre-ind}}$  (°C).

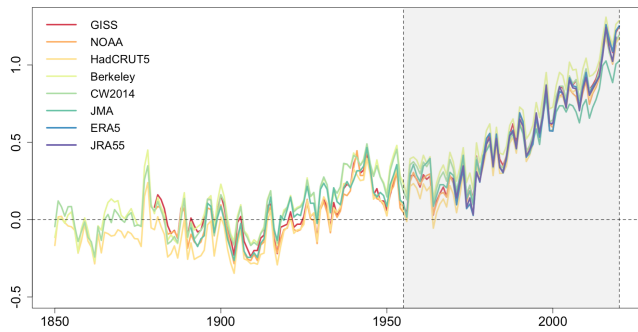
	GISTEMP	NOAA	HadCRUT 5	BEST	CW2014	JMA	ERA-Interim	JRA-55
$\bar{T}_i^{1986-2005}$	0.420	0.445	0.349	0.382	0.305	0.014	0.626	0.635
$\Delta T_{\text{pre-ind}}^{1986-2005}$ (IPCC, 2018)	0.65	0.62	0.60 <sup>a</sup>	0.73	0.65	0.59	-	-
$\bar{T}_i^{\text{pre-ind}}$	-0.230	-0.175	-0.251	-0.210	-0.345	-0.576	-	-

<sup>a</sup> The temperature change  $\Delta T_{\text{pre-ind}}^{1986-2005}$  for the HadCRUT 5 dataset is not available in IPCC (2018), and thus we use that for HadCRUT 4.6 instead.

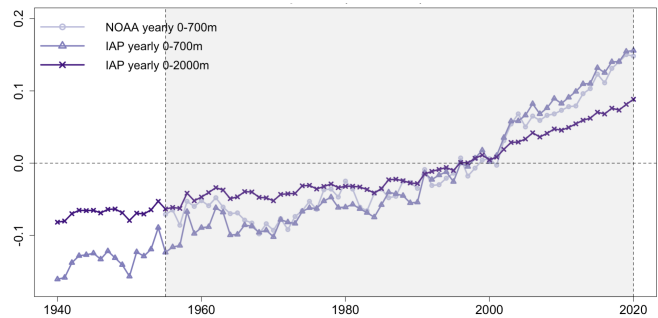
Figure A.1a shows that these eight GMST anomalies after the synchronization have a substantial agreement, especially since the twentieth century. Figures A.1b and A.1c indicate that, after aligning to the same baseline, the NOAA 0-700m ocean temperature and OHC series are also comparable to their counterparts from IAP.

Figure A.1: GMST, ocean temperature, and OHC anomaly series after synchronization. The light gray area corresponds to the time horizon 1955 – 2020 in the empirical study.

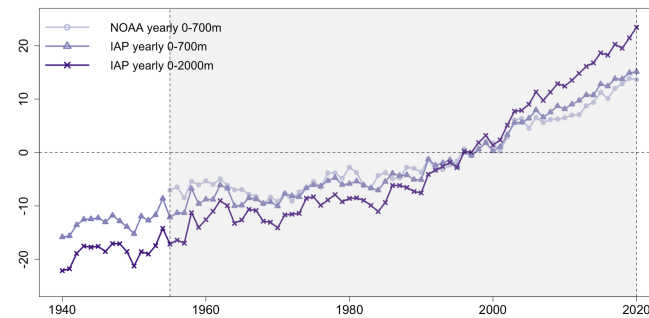
(a) GMST Anomalies ( $^{\circ}\text{C}$ ) (1850 – 2020) with respect to pre-industrial era (1850 – 1900)



(b) ocean temperature ( $^{\circ}\text{C}$ ) (1940 – 2020) with respect to 1981 – 2010



(c) OHC Anomalies ( $\text{J m}^{-2}$ ) (1940 – 2020) with respect to 1981 – 2010



### A.3 Estimation results using one GMST and one pair of ocean temperature and OHC series

Table A.4: Mean estimates of the physical parameters from fitting the EBM-SS base model to different GMST and ocean (ocean temperature + OHC) datasets. The numbers in parentheses are the coefficients of variation.

One ocean temperature and one OHC series are included – 0-700m											
No. of GMST	GMST(s) included	NOAA 0-700m					IAP 0-700m				
		$\bar{\lambda}$	$\hat{\gamma}$	$\bar{C}_m$	$\bar{C}_d$	ECS	$\bar{\lambda}$	$\hat{\gamma}$	$\bar{C}_m$	$\bar{C}_d$	ECS
1 GMST	<b>GISTEMP</b>	0.63 (0.47)	1.45 (0.2)	21.44 (0.38)	96.13 (0.01)	6.24 (0.47)	0.44 (1.1)	1.21 (0.36)	25.52 (0.59)	98.23 (0.002)	8.91 (1.1)
	<b>NOAA</b>	0.82 (0.34)	1.59 (0.21)	18.29 (0.36)	96.14 (0.01)	4.79 (0.34)	0.63 (0.65)	1.31 (0.35)	22.42 (0.55)	98.23 (0.002)	6.19 (0.66)
	<b>HadCRUT5</b>	0.74 (0.41)	1.3 (0.22)	20.3 (0.37)	96.15 (0.01)	5.29 (0.41)	0.63 (0.61)	1.15 (0.3)	22.12 (0.48)	98.23 (0.002)	6.29 (0.62)
	<b>BEST (Berkeley)</b>	0.39 (1.18)	1.56 (0.24)	29.16 (0.59)	96.14 (0.01)	10.09 (1.19)	0.00017 (0.00015)	1.13 (0.29)	43.18 (0.2)	98.23 (0.002)	231033.26 (0.07)
	<b>CW2014</b>	0.55 (0.64)	1.61 (0.21)	26.52 (0.43)	96.13 (0.01)	7.15 (0.65)	0.07 (12.56)	1.21 (0.33)	42.28 (0.72)	98.23 (0.002)	60.06 (12.56)
	<b>JMA</b>	1.01 (0.26)	2.28 (0.21)	15.81 (0.34)	96.13 (0.01)	3.88 (0.27)	0.8 (0.51)	1.83 (0.38)	21.38 (0.61)	98.22 (0.002)	4.93 (0.52)
	<b>ERA5</b>	0.85 (0.32)	1.2 (0.26)	15.8 (0.37)	96.14 (0.01)	4.61 (0.33)	0.87 (0.26)	1.14 (0.27)	14.11 (0.32)	98.22 (0.002)	4.52 (0.27)
	<b>JRA55</b>	0.85 (0.37)	1.32 (0.27)	17.74 (0.43)	96.15 (0.01)	4.61 (0.38)	0.87 (0.3)	1.26 (0.28)	15.85 (0.38)	98.22 (0.002)	4.51 (0.31)
	<b>Median of estimate</b>	0.78		1.51		19.30		96.14		5.03	
	<b>Median of CV</b>	(0.39)		(0.22)		(0.37)		(0.01)		(0.40)	
One ocean temperature and one OHC series are included – 0-2,000m											
No. of GMST	GMST(s) included	IAP 0-2000m									
		$\bar{\lambda}$	$\hat{\gamma}$	$\bar{C}_m$	$\bar{C}_d$	ECS					
1 GMST	<b>GISTEMP</b>	0.18 (1.9)	1.84 (0.18)	21.72 (0.37)	269.28 (0.002)	22.36 (1.9)					
	<b>NOAA</b>	0.33 (1.01)	2.00 (0.19)	19.04 (0.36)	269.28 (0.002)	12.08 (1.01)					
	<b>HadCRUT5</b>	0.25 (1.40)	1.73 (0.20)	20.95 (0.36)	269.28 (0.002)	15.89 (1.40)					
	<b>BEST (Berkeley)</b>	0.03 (14.61)	1.93 (0.19)	27.2 (0.48)	269.28 (0.002)	148.48 (14.61)					
	<b>CW2014</b>	0.10 (3.67)	1.98 (0.19)	26.16 (0.42)	269.28 (0.002)	39.12 (3.67)					
	<b>JMA</b>	0.47 (0.70)	2.65 (0.19)	16.9 (0.35)	269.28 (0.002)	8.44 (0.71)					
	<b>ERA5</b>	0.51 (0.49)	1.55 (0.21)	13.58 (0.27)	269.29 (0.002)	7.64 (0.49)					
	<b>JRA55</b>	0.53 (0.49)	1.7 (0.21)	14.81 (0.3)	269.3 (0.002)	7.44 (0.5)					
	<b>Median of estimate</b>	0.29		1.89		19.99		269.28		13.98	
	<b>Median of CV</b>	(1.20)		(0.19)		(0.36)		(0.002)		(1.21)	

## A.4 Fitted estimates and standardized prediction errors using 0-2,000m ocean series

Figure A.2: Fit of EBM-SS full model to eight GMST series, two 0-700m ocean temperature, two OHC 0-700m, and one radiative forcing series. Panels (a), (c), (e) show the observational series and the smoothed states from the Kalman filter, which are the estimated states conditional on the entire observational paths. Panel (g) shows the fit to OHC series using the assumption  $O = C_d \mu T_d$ . Panels (b), (d), (f), and (g) report the standardized one-step ahead prediction errors. “constant” in the legends of (c) and (g) are the estimated constants for the IAP ocean temperature series.

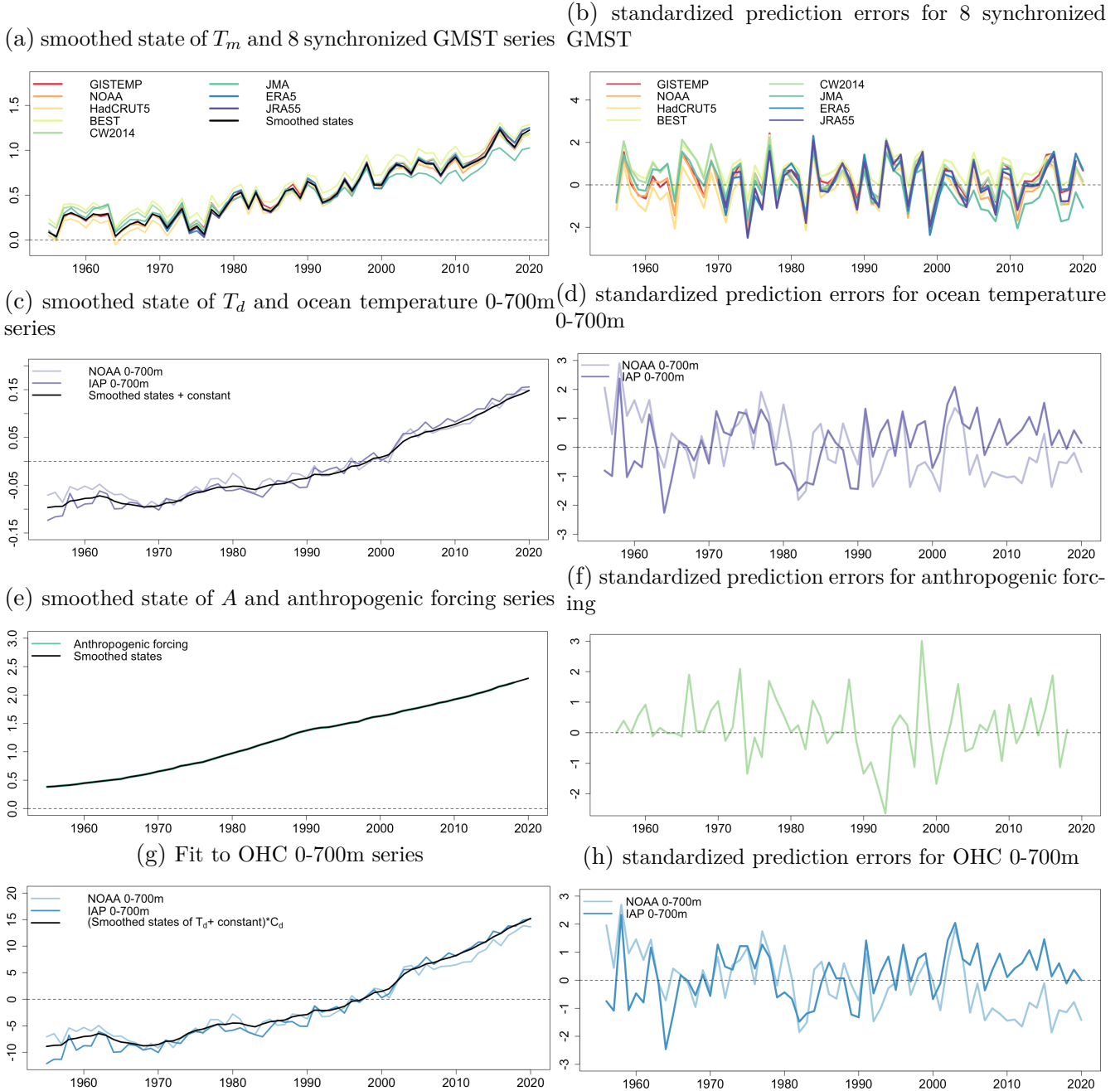
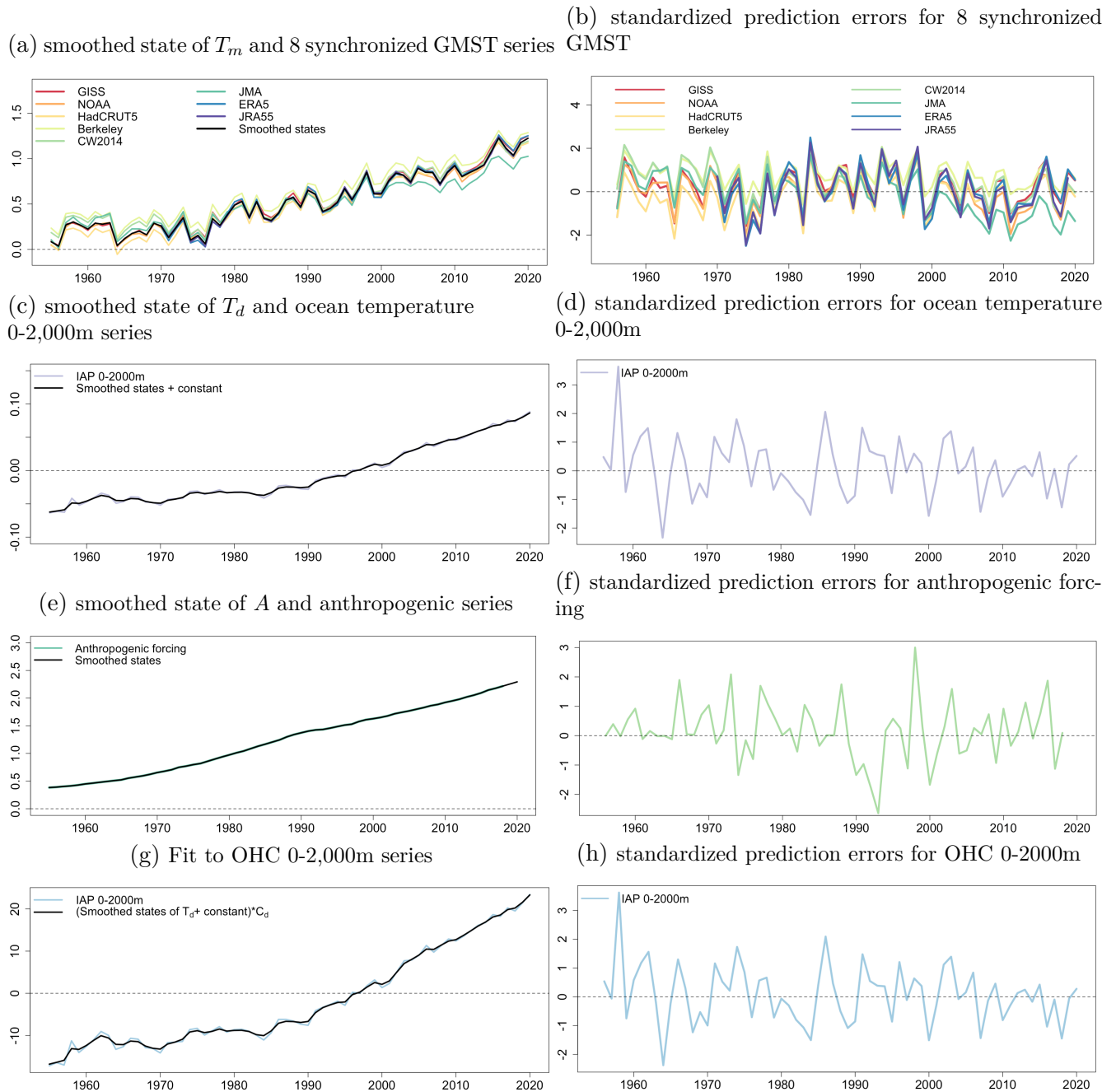


Figure A.3: Fit of EBM-SS full model to eight GMST series, one 0-2,000m ocean temperature, one OHC 0-2,000m, and one radiative forcing series. Panels (a), (c), (e) show the observational series and the smoothed states from the Kalman filter, which are the estimated states conditional on the entire observational paths. Panel (g) shows the fit to OHC series using the assumption  $O = C_d \mu T_d$ . Panels (b), (d), (f), and (g) report the standardized one-step ahead prediction errors. “constant” in the legends of (c) and (g) are the estimated constants for the IAP ocean temperature series.



## A.5 Diagnostic statistics

Table A.5: Diagnostic statistics of the one-step ahead standardized prediction errors for the EBM-SS full model. The upper panel shows the results for 0-700m ocean data. The lower panel shows the results for 0-2,000m ocean data. \*\* and \* denote significance at 1% and 5%.

<b>A. ocean temperature and OHC 0-700m from both NOAA and IAP are included</b>													
	GISTEMP	NOAA	HadCRUT5	BEST	CW14	JMA	JRA55	ERA5	$Y_{T_{d,700\text{ m}}^{\text{NOAA}}}$	$Y_{O_{700\text{ m}}^{\text{NOAA}}}$	$Y_{T_{d,700\text{ m}}^{\text{IAP}}}$	$Y_{O_{700\text{ m}}^{\text{IAP}}}$	forcing
mean	0.284	0.004	-0.225	0.753	0.381	-0.138	0.080	0.045	0.053	0.182	-0.074	0.163	0.149
std	0.945	0.989	0.935	0.724	0.944	0.962	1.067	1.052	1.033	0.930	1.044	0.928	0.989
skewness	-0.102	0.054	-0.115	-0.079	-0.106	0.072	-0.255	-0.160	0.432	-0.167	0.309	-0.180	0.093
kurtosis	2.720	2.598	2.649	2.651	2.612	2.260	2.689	2.427	2.567	2.731	2.444	2.909	3.860
$t_{\text{JB}}^{\text{a}}$	0.325	0.461	0.476	0.399	0.528	1.539	0.759	0.898	2.529	0.498	1.873	0.375	2.034
$Q(1)^{\text{b}}$	4.979*	3.129	4.707*	5.591*	2.533	1.168	2.739*	4.057*	6.076**	3.703	9.895**	2.482	0.000
<b>B. Ocean temperature and OHC 0-2,000m from IAP is included</b>													
	GISTEMP	NOAA	HadCRUT5	BEST	CW14	JMA	JRA55	ERA5	$Y_{T_{d,2,000\text{ m}}^{\text{IAP}}}$	$Y_{O_{2,000\text{ m}}^{\text{IAP}}}$	forcing		
mean	0.259	-0.025	-0.251	0.735	0.358	-0.161	0.065	0.028	0.118	0.089	0.148		
std	0.949	0.985	0.941	0.720	0.937	0.943	1.078	1.056	1.006	1.005	0.988		
skewness	-0.109	0.053	-0.126	-0.093	-0.118	0.086	-0.267	-0.168	0.456	0.483	0.095		
kurtosis	2.703	2.629	2.641	2.660	2.628	2.282	2.719	2.493	4.222	4.289	3.858		
$t_{\text{JB}}$	0.368	0.396	0.520	0.407	0.527	1.478	0.772	0.772	6.290*	7.020*	2.026		
$Q(1)$	4.465*	3.292	4.012*	5.714*	2.880	0.737	2.144	3.737	0.234	0.132	0.000		

<sup>a</sup> Test statistic of the Jarque-Bera normality test (Jarque & Bera, 1980). The null hypothesis is that the sample is normally distributed.

<sup>b</sup> Portmanteau test statistic for serial correlation by Ljung and Box (1978):  $Q(k) = n(n+2) \sum_{j=1}^k \frac{\rho_j^2}{n-j}$ , where  $k$  is the order of lag, and  $\rho_j$  is the sample autocorrelation at lag  $j$ .  $H_0$ : the sample exhibits no serial correlation.